COPROLITES OF THE LATE EOCENE USING VIRTUAL PALEONTOLOGY FROM THE PIPESTONE SPRINGS MAIN POCKET, MONTANA

A Thesis presented to

the Faculty of the Graduate School

at the University of Missouri-Columbia

In Partial Fulfillment

of the Requirements for the Degree

Master of Science

by

Jeremy Louis Webb

Dr. Sarah Jacquet, Thesis Supervisor

MAY 2022

The undersigned, appointed by the dean of the Graduate School, have examined the thesis entitled

COPROLITES OF THE LATE EOCENE USING VIRTUAL PALEONTOLOGY FROM THE PIPESTONE SPRINGS MAIN POCKET, MONTANA

presented by Jeremy L. Webb,

a candidate for the degree of Master of Science,

and hereby certify that, in their opinion, it is worthy of acceptance.

Dr. Sarah Jacquet

Dr. James Schiffbauer

Dr. Tara Selly

Dr. John Huntley

ACKNOWLEDGMENTS

I would like to thank Dr. Andrew Farke, Gabriel Santos, and Bailey Jorgensen from the Raymond M. Alf Museum of Paleontology at the Webb School for gathering and loaning the specimens that were used in this study. Thanks to Dr. Lee Lyman for assistance with the identification of some of the bones extracted from the CT data. I would like to thank my colleagues at the University of Missouri Department of Geological Sciences for their support in completing this thesis. I would especially like to thank Drs Tara Selly, Jim Schiffbauer, and John Huntley for their time and expertise and for serving on my committee. Finally, I would like to thank Dr. Sarah Jacquet for being my advisor and guiding me not only through the thesis process but also graduate school as a whole.

Funding: University of Missouri Research Council Award #URC-20-046

TABLE OF CONTENTS

LIST OF FIGURES

LIST OF TABLES

ABSTRACT

The study of coprolites and their internal constituents has previously employed a predominantly destructive means of extraction, resulting in the partial or complete loss of the specimen. Recently, however, there have been several studies adopting a more modern approach to data collection and analysis, incorporating three-dimensional imaging techniques such as x-ray tomographic microscopy (µCT) and synchrotron microtomography. These non-destructive methods allow us to virtually extract qualitative information on the identity, structure, orientation, and size of inclusions, as well as important quantitative information with respect to the relative proportions of inclusions to matrix.

Herein, µCT was used to study bone, and other miscellaneous inclusions, in two size classes of coprolites from the Eocene Pipestone Springs Main Pocket (PSMP) assemblage (Renova Formation), Montana. Segmentation of µCT-scans has enabled documentation of the degree of skeletal fragmentation and proportion of bone material to the phosphatic matrix which provides novel insights into the feeding behavior of the producer and taphonomy of constituents. Among the features identified in the µCT data were skeletal fragments, including those showing evidence of bone-crushing; delicate molds of hair; lithic fragments encrusted on the coprolite surface; and lastly several pores and cracks throughout the coprolites' structure. A benefit of this technique is the ability to extract quantitative data on bone volumes and diameters for statistical comparison between the two different size classes of coprolite. In combination with volume renders of the segmented material, we also adopt more traditional methods such as thin-section

petrography and scanning electron microscopy with energy dispersive spectroscopy (SEM-EDS) to characterize the compositional and taphonomic attributes of the samples. We emphasize that traditional methods are not obsolete, as they provide data that cannot be obtained using digital methods. X-ray microscopy compliments traditional methods insofar that areas of interest can be identified prior to destructive sampling. Overall, this combined approach has provided a means to observe and statistically test differences in the coprolite gross morphology and their inclusions across the two size classes thereby offering valuable insights into the broader paleoecology of the PSMP coprolite producers.

CHAPTER 1: INTRODUCTION

1.0 Coprolites: trace fossils and terminology

Coprolites are a form of trace fossil produced by the fossilization of animal feces, and consequently are important in understanding aspects of the producer's behavior concerning consumption (e.g., diet and mastication), digestion, and excretion (Hunt et al. 2012). Particularly among vertebrates, behavioral and morphological adaptations for food consumption are diverse. Excluding taphonomic features, the contents and morphologies of the feces produced will be tied to the anatomy and feeding behavior of the coprolite producer. Notably, coprolites can reveal more than just the individual's behavior, rather they provide a broader insight into the intimate relationships between the producer and their ecosystem. From this information, it is possible to extrapolate the wider functionality of ancient food webs in a manner that most other fossil remains cannot. Moreover, coprolites can represent sites of exceptional preservation (i.e., Konservat-Lagerstätten) exhibiting near-perfect preservation of organisms or tissues that would not normally enter the fossil record (Qvarnström et al. 2016). In exceptional circumstances, coprolites have preserved soft tissues including muscle, hair, feathers, bacteria, and intestinal parasites (Meng and Wyss, 1997; Hugot et al. 2014; Qvarnström et al. 2016). More common inclusions include arthropod exoskeletons, fungi, pollen, and spores. In general, feces produced by carnivores are more likely to be preserved due to the high phosphorous content associated with skeletal and soft tissue material ingested and the

specific microbial microenvironment which assists with early lithification (Qvarnström et al. 2016). Whilst the application of coprolites in paleontological studies such as biostratigraphy are notably limited (e.g., by sample size, homomorphism, extramorphological variations, and a bias towards carnivorous producers (Hunt et al. 2012)), these disadvantages do not discredit their use in paleoecological studies for understanding the behaviors of extinct organisms and habitats they occupied.

Similar to other subfields of ichnology, the study of coprolites has developed a parataxonomy with which to describe and discern the vast morphological variation that exists across potential producers separated by time and space. The term 'coprolite' was first introduced in 1829 by William Buckland in "XII. —On the Discovery of Coprolites, or Fossil Fæces, in the Lias at Lyme Regis, and in other Formations". Since then, coprolite terminology has developed sporadically in conjunction with the advancement of the discipline, though the definition of a coprolite *sensu stricto* persists specifically as the formation of fossilized feces (Hunt et al. 2012). Neumayer (1904) was the first to introduce terminology to describe the overall shapes of spiral coprolites, which he separated into heteropolar and amphiopolar forms after observing samples from the early Permian of Texas (Hunt and Lucas, 2012). Heteropolar coprolites are described as having large, variable-sized spirals, closely compacted on the surface, and focused on one end of the coprolite. Amphipolar forms are characterized by a small number of spirals that are more evenly spaced out throughout the coprolite (Neumayer, 1904; Hunt and Lucas, 2012; Hunt et al. 2012). Non-spiral coprolite morphotypes are more relevant to the case study in the present contribution. Such morphologies are fairly simple, consisting of cylinders of varying lengths with rounded terminations. Several attempts to sort simple coprolite

morphotypes have been founded on classification schemes used in the identification of modern scat (Häntzschel et al., 1968; Murie, 1974; Stuart and Stuart, 2000; Chame, 2003; Hunt and Lucas, 2012). These serve as useful guides but authors caution that some taxa are known to produce more than one morphotype, a problem that persist across the discipline of ichnology. Moreover, Hunt and Lucas (2012) emphasize the need for a disciplinary separation in the systematic terminology used for modern scat and that of fossilized remains.

Vernacular used in the description of non-spiral coprolites is focused on the terminations and constrictions along the length of the feces. Terminations tend to be either broadly rounded (typical of the posterior end that emerges first from the anus) or tapered to a point (the result of pinching the trailing anterior end with constriction of the anal margin) (Thulborn, 1991; Hunt and Lucas, 2012). Thulborn (1991) differentiated forms with dissimilar terminal morphologies as *anisopolar*, and those with similar terminal morphologies as *isopolar*. In such cases where coprolites are composed of several sub-units, the individual components are referred to as *segments* (Hunt and Lucas, 2012). Another term used in the comparative morphology of coprolites is *homomorphism*, which is used to describe coprolites that appear similar but that vary in structure or contents (Horner and Hanson, 2019). Meanwhile, *extramorphological* variations indicate disparity caused by taphonomonic processes or the depositional environment (Horner and Hanson, 2019).

The terminology and classification of vertebrate coprolites has undergone several reiterations with expanded classification schemes incorporating associated trace fossils (Hunt et al. 2012). However, following initial attempts to separate out such trace fossils

based on their respective origins, a number of overlapping terms were introduced. In a recent review, Hunt and Lucas (2012b) attempt to clarify the definition and usage of certain terms by establishing new levels of higher-order classification (Fig. 1.1). For instance, the term *bromalite* is now an inclusive term used to describe trace fossils representative of food items that have been orally or rectally expelled, or retained *in situ* within the organism (Hunt, 1992). Bromalites are further divided into several subcategories. These were originally limited to coprolites *sensu stricto*, cololites, and regurgitalites (Hunt, 1992), however the list now incorporates nine additional second-order terms (see Hunt and Lucas 2012b, Table 1 therein). Alternatively, other first order terms include *demalite*, *cumulite*, *gignolite* and *gastrolith*, which excluding the cumulites are summarized in Figure 1.1. Cumulites are accumulations of organic or inorganic material concentrated by an organism (i.e., a food cache) and gastroliths are nondigestible objects of no calorific value (Hunt, 2012).

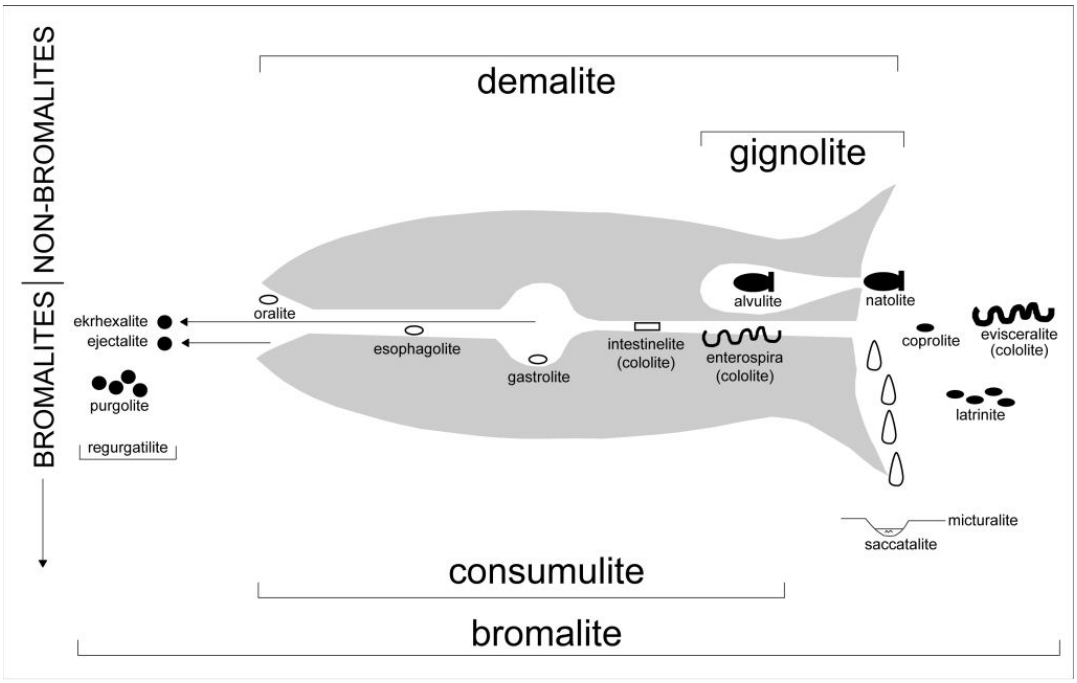

Fig. 1.1. Terminology related to bromalites (food consumption) and other associated trace fossils, including gignolites (reproductive) and demalite (fossil material preserved in the body cavity but not derived from the organism). (Modified after Hunt et al. 2012, fig. 1)

1.1 Background and new advances in coprolite studies

William Buckland was the first to identify these fossiliferous remains as trace fossils based on observations of extinct hyena feces recovered from Kirkdale Cave, North Yorkshire, England (Buckland, 1822, 1824). Although the documentation of coprolites extends almost a century prior to Buckland's seminal work, these trace fossil remains were frequently misidentified as having a botanical origin (e.g., fossilized larch cones, nuts, etc.), some relation to corals, and curiously were also compared with 'Bezoar stones'—concretions formed in the stomach of the Bezoar Ibexes (Duffin, 2009). After an initial burst of studies from Buckland (1829a, b; 1835), coprolites fell into obscurity in the paleontological literature and were subject to minimal research, with most studies being relegated to exploration for sources of phosphate for fertilizer production (Hunt et al. 2012). Despite an initial paucity of studies into these elusive fossil remains, there was an uptick in papers published in the early 1900s as human coprolites were suggested to be an important field of study (Hunt et al. 2012).

As noted above, the work of Neumayer (1904) and Hoernes (1904) provided a foundation in terminology and classification of coprolites. In 1929, the first paper describing human coprolites was published (Loud and Harrington, 1929), sparking an interest and leading to several developments in the discipline. Among the founding contributions in this new avenue of research was a study investigating coprolites affiliated with native populations of Peruvians (Callen and Cameron, 1955). Callen and Cameron (1955) sought evidence of human parasites in preserved feces to gain insight

into parasite diversity within the native population and whether these organisms were also responsible for crop failures in the area. The first challenge the authors faced was rehydrating the coprolites so they could be more easily mechanically prepared without damaging parasite remains within the sample (Callen and Cameron, 1955). This was achieved by soaking the dried coprolite in a solution of trisodium phosphate which facilitated extraction of preserved soft animal and plant tissues. While they did not find evidence of preserved parasites, they identified several well-preserved macrofossil inclusions (i.e., plant remains, bone) that reflected the native people's diet (Callen and Cameron, 1955). Recognizing the potential such methods could afford in the study of ancient diet, climate, and parasitic relationships led to a renewed interest in desiccated Pleistocene animal and human coprolites, with several researchers dedicated to the field up until the 1990s (Hunt et al. 2012; Shillito et al. 2020).

Coprolites did not receive much study in wider vertebrate paleontology circles until the 1990s (Häntzschel et al. 1968; Hunt et al. 2012), with the exception of Paleozoic fish workers focused on reconstructing the paleoecology of Pennsylvanian shark species (Zangerl and Richardson, 1963; Williams, 1972). As interest in human coprolites wanned, a new direction of research emerged principally investigating how coprolites could inform on animal behavior and diet of pre-Pleistocene organisms. A rise in studies focused on dinosaur coprolites between the 1990's to 2000's gave way to deep-time studies examining their trophic relationships and feeding behaviors (Hunt et al. 2012). For example, Chin and colleagues made notable contributions into the behaviors of dinosaurs and their food webs through studies on dung beetle activity and muscle tissue preservation in Cretaceous coprolites (Chin and Gill 1996, Chin et al. 2003).

Up to this point, the study of coprolites has principally employed a suite of macroscopic, microscopic, and (more recently) biomolecular approaches to extract information on producer identity, diet, and habitat (Shillito et al., 2020). Many of the founding studies documented coprolite macromophology (i.e., size and shape) using illustrations which were later superseded by standard light and stereo microscopy to aid in identification of features that were otherwise visible with the naked eye. However, with the prospect of novel information from coprolite inclusions, techniques involving more destructive or consumptive sampling were used to access this material. Usually on a subset of the coprolite sample, these internal components have been examined via disaggregation following rehydration (Callen and Cameron, 1960) or mechanical crushing (Roust, 1967). Issues in damaging delicate specimens have reduced the implementation of the latter. Once separated, inclusions or other material can then be further examined using high powered imaging techniques such as Scanning Electron Microscopy (SEM). These methods are frequently supplemented with thin section petrography to provide insight on the relative proportions of inclusions and the micromorphology of the sample overall.

The procedures outlined above have become part of a standardized workflow for paleontological coprolite samples, though archaeological studies examining human and associated domesticates have also facilitated DNA sequencing and lipid analysis due to the relative stability of the molecules (Shillito et al. 2020). Analysis on faecol sterols and dietary sterols further allows for the determination of whether a coprolite sample could be attributed to a carnivore, omnivore, or herbivore. Proteins have also shown to preserve in coprolites and have been teased out using cytochemical staining (Shillito et al. 2020).

Many of these biomolecular methods are restricted to use on archaeological datasets (<10,000 years old), though there is potential for the application of biomarkers in paleontological specimens. Moreover, one of the more notable technical advancements in the study of coprolites coincides with developments in high powered imaging techniques, principally x-ray microscopy (e.g., X-ray Tomographic Microscopy and Synchrotron Microtomography).

Virtual paleontology—the three-dimensional study of fossils through digital visualization and reconstruction (Sutton et al. 2003)—presents a novel avenue in the examination of macro- and micromorpholgy of the internal components of coprolite samples. Despite the paleoecological importance of coprolites, and the wealth of information that their inclusions can provide, there has been a surprising scarcity of studies investigating these features by means of non-destructive three-dimensional imaging techniques. The few studies which exist have demonstrated there is significant potential in their application (Rasmussen, 2014; Holgado et al. 2015; Wang et al. 2018; Abella et al. 2021). Such methods enable researchers to observe features, internal structures, microstructures, and other inclusions that would not otherwise be obtainable using traditional methods (Wang et al. 2018). These prior studies are, however, limited in scope and mainly focus on the taxonomic aspects of the macroscopic inclusions (frequently bone material), and overlook the broader taphonomic information from a more holistic perspective. This contribution aims to implement these more standardized methods in combination with x-ray tomographic microscopy (μCT) to elucidate the various macroscopic and microscopic features within a taphonomic framework.

CHAPTER 2:

EOCENE COPROLITES FROM PIPESTONE SPRINGS MAIN POCKET, SOUTHWEST MONTANA

2.0 Introduction

In this chapter, we employ non-destructive x-ray tomographic microscopy (µCT) in conjunction with targeted consumptive sampling to gain a more holistic view of the internal composition and inclusions of a select coprolite assemblage. The coprolites studied were recovered from the Pipestone Springs Main Pocket (PSMP) assemblage (Renova Formation), Montana. PSMP falls within the Late Eocene-Chadronian age, estimated at an age of 38 Ma to 33.9 Ma. The environment supported a wide range of mammal life, including both large and small predators (Lofgren et al. 2017). Previous work on this material has focused on identifying the vertebrate inclusions and the likely identity of the producer. Lofgren and colleagues examined surface morphology and visible skeletal elements of the coprolites were examined in 358 specimens, in addition to 20 specimens that were mechanically prepared by removing skeletal inclusions. A survey of the measurable dimensions of this coprolite assemblage revealed two distinct size classes, with smaller forms ranging from 4–15mm in diameter and larger forms ranging from 16–29mm in diameter (Lofgren et al. 2017). Consequently, these are inferred to have been produced by different organisms. The larger coprolites are suggested to have been produced by a member of the genus *Hyaenodon*, large terrestrial predators found in Eurasia and North America during the middle Eocene to the early Miocene (Wang et al. 2005). The producer of the smaller class of coprolites could not be attributed to any

single genus but is suggested to have been produced by potentially several smaller carnivorous taxa including *Daphoenictis tedfordi*, *Palaeogale sectorial*, and members of *Dinictis* (Lofgren et al. 2017). This work provides an important foundation from which we can ascertain the broader palaeoecological framework for this coprolite assemblage.

Advanced imaging techniques provide a novel avenue of investigation into a sub-set of the PSMP coprolites. This allows us to corroborate previous findings on the gross morphology of the coprolites, as well as to (1) visualize overall specimen structure and identify the undigested skeletal and keratinous inclusions via virtual segmentation; (2) quantify the relative proportions of bone inclusions and pores to feces matrix; and (3) discern any difference between the two size classes with respect to the shape and volume of bone inclusions. By expanding on previous findings and those presented here, we seek to elucidate the feeding behavior of the ancient vertebrate producers and their corresponding size class coprolites found within the PSMP assemblage. In addition, this work serves to assess the potential application of µCT techniques in the analysis of coprolites compared to more destructive methods.

2.1 Locality and Geological Setting

Coprolites are derived from the Pipestone Springs Main Pocket (PSMP), considered part of the Climbing Arrow Member of the Renova Formation in Jefferson County, Montana (Kuenzi and Fields, 1971; Fig. 2.1A and B). Specimens assigned to the Pipestone Springs Main Pocket are affiliated with three smaller fossiliferous sections located at section 29, T2N, R5W, about 2.4 kilometers away from Pipestone Hot Spring (Tabrum et al. 1996). There are also isolated pockets that are attributed to the PSMP, including Montana MV

5811, which has produced the largest number of specimens in the area, and MV 5908 (referred to as Pipestone Spring South) about 229 meters away from the main assemblage (Tabrum et al. 1996). Specimens collected and documented herein are equivalent to the MV 5811 locality, though both isolated pockets are lithologically and faunally indistinguishable, and they are often referred to as the same bed (Tabrum et al. 1997). The MV 5811 locality is situated on the prominent dip slope towards the northern end of the Main Pocket exposures (Orr, 1958; Fig. 2.1C).

Based on prior biostratigraphic correlation and magnetostratigraphy (Prothero, 1984), the PSMP assemblage has been estimated as middle to late Chadronian in age (35.0–35.5 Ma). The deposit is exposed as a 50 cm–4 m thick layer of homogenous tuffaceous mudstone, lacking sedimentary structures or obvious bioturbation (Lofgren et al. 2017; Fig. 2.1D). Coprolite and vertebrate remains are randomly distributed throughout the deposit, both laterally and vertically, precluding hydrodynamic sorting (Lofgren et al. 2017). The conditions in which these deposits formed remain inconclusive, however, Lofgren et al. (2017) proposed two scenarios involving either repeated ash-rich mud flows or inundated floodplain deposits.

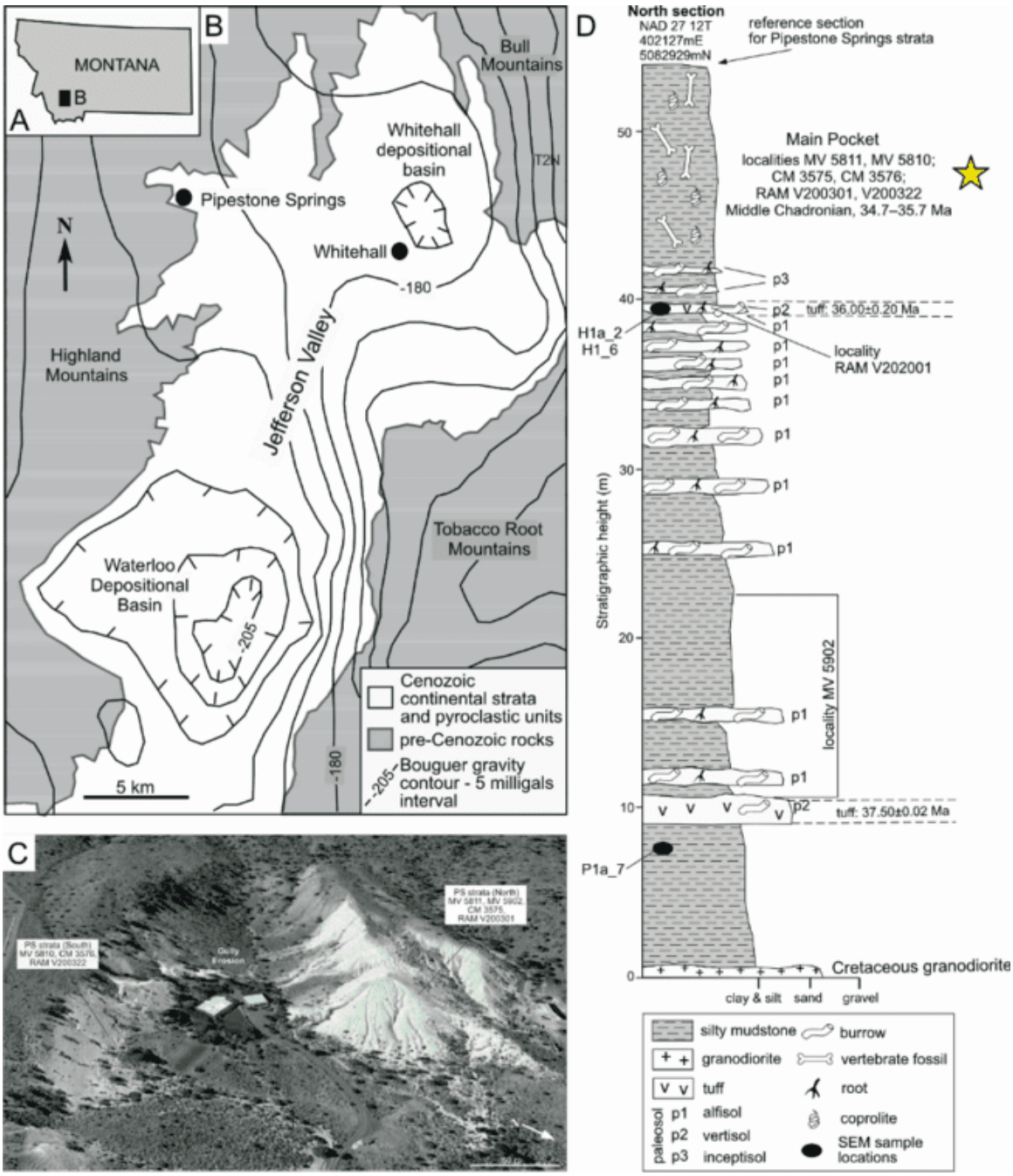

Figure 2.1. A. Geographic position of the locality site in Montana. **B.** Simplified geologic map of the Cenozoic deposits in the Upper Jefferson Valley and the locality of the Pipestones Spring Reference section and sites sampled. **C.** Arial photography of the North and South sections of the Pipestone springs areas. **D.** Stratigraphic section of the reference section for the Pipestone Springs Main Pocket. Modified after Hanneman et al. (2022).

2.2 Methods

The twelve coprolite specimens examined in this chapter (see Table 1) are housed in the collections of the Raymond M. Alf Museum of Paleontology, Claremont, California. The external appearance of the coprolites was examined using reflective light microscopy and photographed using a GIGAMacro Magnify2 Robotic Imaging System with Canon EOS Rebel T6i/T8i DSLR cameras to acquire gigapixel resolution photomosaics. Exterior physical features were described using the methods outlined in Jouy-Avantin et al. (2003), including noting color, shape, hardness, texture, as well as the presence or absence of constrictions, inclusions visible at the surface, and taphonomic modifications of the coprolites. Coprolite color was characterized based on the Munsell Color Rock-Color Chart (Munsell Color, 2010). The overall shape and specific morphology of the coprolite extremities were noted (e.g., sharp-ended, rounded, or broken), as were taphonomic modifications including gallery holes, vacuoles, fissures, desiccation, abrasion, and surface markings/burrows. Any inclusions visible on the surface were also noted (i.e., bones, adhering sediment). The texture was examined to determine whether the coprolite displayed homogenous or heterogeneous mixtures; compacted aggregates less than 1 mm, compacted aggregates greater than or equal to 1 mm, homogenous mixtures with some aggregates, or many aggregates included in a homogenous mixture.

2.2.1 *X-ray tomographic microscopy and 3D visualization*

Coprolites samples were scanned using a Zeiss Xradia 510 Versa µCT microscope at the X-ray Microanalysis Core (MizzoµX), University of Missouri for non-destructive analyses. Optimal scanning parameters for the coprolites varied, with source voltage ranging between 80kV to 140kV, source power between 7W to 10W, and exposure time

between 1 to 5 second(s). All scans captured 1601 projections and used a 0.4x objective detector. Two types of filters were used, both of which were low-energy filters, with 12 scans using the LE5 filter, and two using a LE2 filter. Voxel size ranged from 3.4618 µm to 30.12 µm. A summary of the scanning parameters used for each sample are summarized in Appendix Table 1.

Segmentation and visualization of the three-dimensional data were achieved by importing serial tomograph stacks into Dragonfly software v. 2020.2 Build 941v. 2022.1 for Windows, Object Research Systems (ORS) Inc, Montreal, Canada, 2018 (http://www.theobjects.com/dragonfly). Segmentation was performed using a greyscale threshold and manual segmentation to extract internal constituents and features of the coprolites (i.e., bones and pore spaces), as well as the matrix. Volumes of the coprolite, pore space, and bone inclusions for the respectively labeled voxels and their relative proportions within the coprolite were calculated. Feret diameters (i.e., caliper diameter; the distance (maximum and minimum) between two points at an arbitrary angle) for the bones and pores were exported using the bone and pore layers created within Dragonfly. Thresholds were set to focus the data more with a minimum feret diameter for bones being set at 0.14 mm and the minimum feret diameter for pores being set at 0.196 millimeters. A multi-ROI was extracted from the bone segmentation to group labeled voxels into individual bone components. Select components were then extracted as meshes (.stl files) and smoothed for one iteration in Dragonfly before being exported to Meshmixer [Autodesk Meshmixer 3.5]. 3D meshes were rendered to remove islands and unrelated material and applied with a shader. Each bone was examined individually for identification and to determine the general shape and signs of fragmentation.

2.2.2 *Statistical Analysis*

Analyses were conducted using software package *R* (R core Team, 2014; Version 4.1.0) and figures were produced using R packages *ggplot2* and *ggthemes* (Wickham, 2016; Arnold, 2021). Raw data is provided in Tables 4 and 5 in the Supplement Materials along with *R* scripts. Using the volumetric data in Table 2 in the Supplement Material, two bar graphs were produced in Microsoft Excel; the first showing the respective contributions of matrix, bones, and pores to total coprolite volume (converted to cm^3 for ease of comparison), and the second showing the relative proportions of these three components for each of the samples.

2.2.3 *SEM and EDS analysis*

A single specimen (RAM 17540) was prepared and sectioned for examination via optical and scanning electron microscopy. The coprolite was impregnated with PALEObond Penetrant Stabilizer to prevent the coprolite from fracturing or breaking during the sectioning process. Subsequently, the sample was embedded in epoxy and cut diagonally along a predetermined line obtained from the µCT data. One of the two halves was polished using a Buehler EcoMet250, while the other was left unpolished. Both halves of the sample were then analyzed via SEM using a Zeiss Sigma 500 VP at MizzoµX. The cut surface of this sample was imaged using the ATLAS workflow for large area SEM mosaics using the high-definition 5-segment backscattered electron detector (as secondary imaging would likely not provide significant information on cut or polished surfaces). Following ATLAS mosaic construction, elemental mapping was conducted on specific regions of interest using dual Bruker XFlash energy dispersive X-

ray spectrometers (EDS). All SEM analyses were conducted at the following operating conditions: 20 keV beam accelerating voltage, 40 nA beam current, 60 µm aperture for imaging (120 µm aperture for EDS elemental mapping), chamber pressure at 20 Pa, and a working distance of 16.5 mm.

2.3 Results

2.3.1 *Coprolite External morphology*

The coprolites were divided into the two different classes as defined by Lofgren et al. 2017: the larger class coprolites (Class I; n=7), include RAM 17370, 17405, 17517, 17540, 17546, 17547, and RAM 18171; the smaller coprolites (Class II; n=5) include RAM 17557, 31209, 31211, 31212, and 31214. Key measurements (i.e., mass, length, and width) are summarized in Table 1. The coprolites exhibited three different colors, including 5Y 7/2 (yellow gray), 5Y 8/4 (grayish yellow), or 5Y 8/1 (yellowish gray) of the Munsell Color Chart (2010). There was no obvious color difference between the classes of coprolites, though all Class II coprolites show 5Y 8/1.

Most Class I coprolites have a smooth, relatively homogenous surface and tend to share a similar cylinder-like shape, circular in cross-section though occasionally flattened on one side (i.e., RAM 17517) (Fig. 2.2). Notable exceptions include RAM 17547 (Fig. 2.2E) and RAM 17546 (Fig. 2.2G), which both display a rough, topographically complex surface, while simultaneously showing signs of constrictions. Class II coprolites also have homogenous, smooth surfaces but are less uniform in shape. As noted by Lofgren et al (2017), the smaller forms exhibit blunt or tapered ends, and occasionally both. Both classes of coprolites have bone inclusions on their surface, which could be identified as

small black inclusions that are visible by the naked eye. In-depth descriptions of each specimen are included as follows. These are ordered from largest to smallest in terms of total coprolite mass.

Table 1. Coprolite dimensions and weight arranged by size Class and mass (g).

Class	Sample Name	Length (mm)	Width (mm)	Mass (g)
Class I	RAM 18171	64.36	24.03	39.14
Class I	RAM 17517	50.69	24.11	33.22
Class I	RAM 17540	45.94	23.19	27.75
Class I	RAM 17405	44.81	22.15	22.00
Class I	RAM 17547	28.89	28.90	19.19
Class I	RAM 17546	42.50	20.55	17.65
Class I	RAM 17370	39.97	21.56	15.97
Class II	RAM 17557	26.14	11.05	3.61
Class II	RAM 31214	24.03	10.71	3.27
Class II	RAM 31312	26.30	10.63	2.57
Class II	RAM 31211	22.65	9.91	2.08
Class II	RAM 31209	14.38	11.26	1.68

RAM 18171: The specimen is yellowish-grey (5Y 8/1) and has a defined cylindrical shape, with relatively flat edges leading into a pointed extremity on one end and blunt fractured extremity on the other (Fig. 2.2A). There are few inclusions visible on the surface of the coprolite. The texture is homogenous and smooth with very little variation. The broken extremity displays a courser texture indicating that the interior composition of the coprolite differs from the exterior surface of the coprolite.

RAM 17517: Primary yellowish-grey (5Y 8/1), the surface of the coprolite appears homogeneous and smooth on one side (right; Fig. 2.2B) while the opposite side (left; Fig. 2.2B) displays a more irregular surface. The rougher side appears to have enlarged cavities and pitting that differ from fractures as they do not expose any interior structure

of the coprolite. One extremity has a slightly rounded point that is offset from the central long axis. The other extremity is poorly preserved and may be weathered, resulting in a blunt and irregular surface There are no obvious inclusions on the surface of the coprolite.

RAM 17540: Two main colors are present including yellowish-grey (5Y 8/1) and pale greenish-yellow (10Y 8/2). The entire coprolite is preserved as a cylindrical form with varying shapes in extremities and a homogeneous matrix (Fig. 2.2C). In sum, one end is more pointed off-center than the other, with the latter evenly rounded. Visible bone inclusions at the surface are seen closer to the more pointed end of the coprolite.

RAM 17405: Yellowish-grey (5Y 8/1) in color, the coprolite is cylindrical. Similar to RAM 17517, the surface of one side (left; Fig. 2.2D) of the coprolite is smooth and homogeneous while the other (right; Fig. 2.2D) has small cavities that create a slightly rougher texture comparatively. The center of the coprolite has a tear line going through the entire surface. This does not appear to be some sort of constriction as there is no obvious change in the coprolite's shape along that tear. One extremity of the coprolite is rounded (top; Fig. 2.2D), creating a blunt point while the opposite extremity has no distinct shape and is comparatively rough indicating weathering but not fracture.

RAM 17547: Yellowish-grey (5Y 8/1) in color, the coprolite is clearly broken, missing a significant portion at one end (Fig. 2.2E). Given the parallel sides leading to the fractured end, the complete specimen would likely have been cylindrical. The only developed extremity is evenly rounded. The exterior texture is very smooth with some noticeable abrasions and localized compression on the surface. There are no inclusions on the

exterior surface or the broken surface, the texture of the coprolite was entirely homogeneous.

RAM 17546: Grayish-yellow (5Y 8/4) in color, the specimen appears entirely preserved but with minor damage on either of the rounded extremities of the coprolite (Fig. 2.2F). The coprolite outline is irregular, composed of three rounded segments differentiated by two constrictions that were cemented together during the lithification process. The matrix of the coprolite appears to be homogeneous with some very fine aggregates, however, the texture is more porous with distinct spherical pores across the surface but concentrated around the center of the coprolite. There are no obvious inclusions on the exterior of the coprolite.

RAM 17370: Yellowish-grey (5Y 8/1) in color, the coprolite has a porous texture comparable to RAM 17546 with several pores on the surface but also evidence of abrasion due to the more irregular surface (Fig. 2.2G). There is a large hole in the surface, ~2 mm by 1 mm in diameter. The coprolite appears to be two different near-spherical segments, divided roughly in the middle of the coprolite. Bone inclusions are visible on the more porous surfaces of the coprolite. The extremities are mostly rounded with one more pointed comparatively.

RAM 17577: Yellowish-grey (5Y 8/1) in color, the coprolite is mostly intact with some minor damage on one of the extremities. The shape of the coprolite is cylindrical with a well-defined pointed extremity at one end (Fig. 2.2H). The damage on the opposite extremity permits examination of some inclusions within the specimen. These inclusions appear to be small bone fragments, lacking a distinct shape and extending deeper into the

coprolite matrix. The texture of the coprolite is homogeneous, punctuated by occasional small holes. These small holes vary in size, ranging between 0.5 and 1.0 mm.

RAM 31214: Yellowish-grey (5Y 8/1) and appears completely intact. The overall shape is a clearly defined cylinder, with both extremities being just slightly rounded (Fig. 2.2I). The surface texture of the coprolite is relatively smooth with minor cracks, and no visible inclusions. The texture is predominantly homogenous with few aggregates represented by black spots dotted around the coprolite.

RAM 31212: Yellowish-grey (5Y 8/1) in color, shape is distinctly lanceolate in shape. While both extremities are pointed, one is significantly shorter while the other tapers gradually to a point (Fig. 2.2J). Bone inclusions are visible near both extremities and focused towards the shorter end. The texture of the coprolite is homogenous, though the coprolite has many small cracks and grooves along the tapered end (Fig. 2.2J).

RAM 31211: Yellowish-grey (5Y 8/1) and appears almost entirely intact except for a small portion on one extremity. The texture of the coprolite is homogenous with noticeable tears which manifest as small imprints on the coprolite surface (Fig. 2.2K). The opposite extremity (bottom, Fig. 2.2K) also exhibits a blunt point. There are no noticeable inclusions on the exterior surface.

RAM 31209: Yellowish-grey (5Y 8/1) in color, the shape appears sub-spherical with one extremity notably pointed compared to the other extremity, which is more rounded (Fig. 2.2L). The texture of the coprolite is homogenous, but with a few small cavities (0.5–1.3 mm), but do not reveal any sort of inclusions in the coprolite.

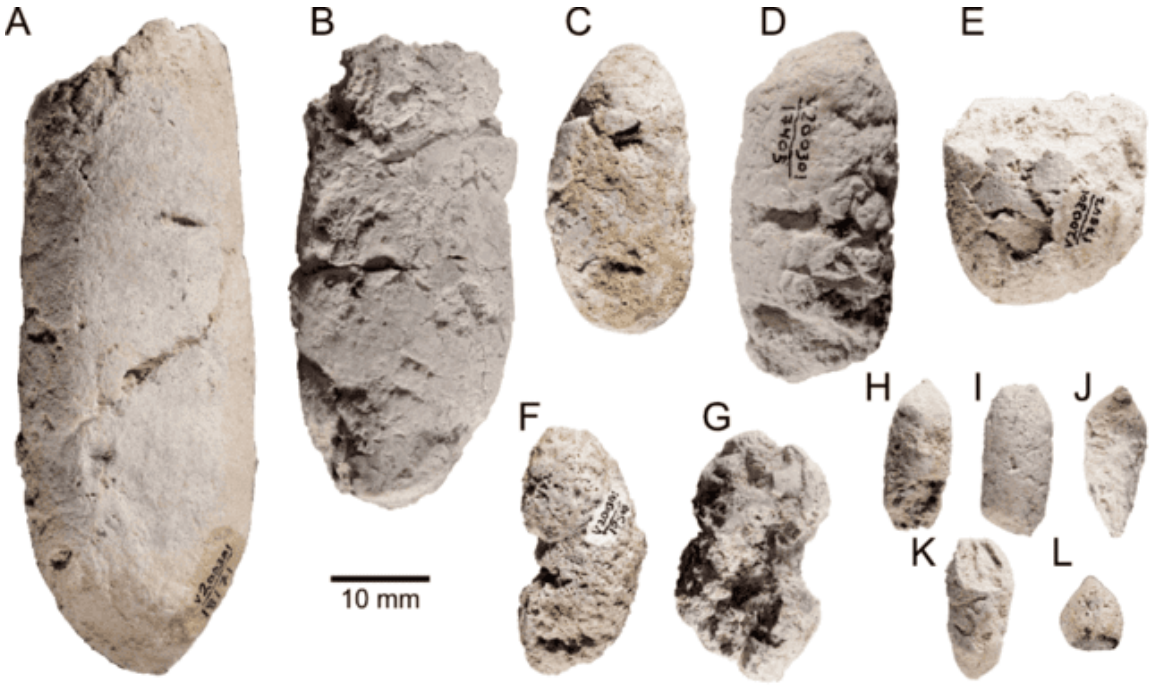

Figure 2.2. Coprolites arranged by mass (g) into Class I (A–G) and Class II (H–L). **A.** RAM 18171. **B.** RAM 17517. **C.** RAM 17540. **D.** RAM 17405. **E.** RAM 17547. **F.** RAM 17546. **G.** RAM 17370. **H.** RAM 17557. **I.** RAM 31214 **J.** RAM 31212 **K.** RAM 31211 **L**. RAM 31209.

2.3.2 *Taphonomic surface features*

2.3.2.1 Desiccation Cracks

Desiccation cracks occur prior to lithification of the coprolite and are caused in response to the climate and depositional environment (Northwood, 2005). Several samples displayed desiccation cracks on the exterior coprolite surface to varying degrees (Table 2). An example of these features can be seen on RAM 17517 (Fig. 2.3A), where the cracks appear as small continuous lines that disrupt the sample's surface. RAM 18171 also displays large, infilled cracks approximately midway along the sagittal length that range from 3–10 mm in length (Fig. 2.2A). Desiccation cracks can vary in quality and size from large, conspicuous cracks with infilled sediment to small hair-line cracks on the surface of the coprolite.

2.3.2.2 *Abrasion*

Surface abrasion was common, with most samples (N=8) displaying evidence of significant abrasion (Table 2). Abrasion relates to how smooth the surface has become in response to erosion caused by water or wind-born particle scouring following excretion or transport and weathering post lithification (Northwood, 2005). We employ the three categories designated by Northwood (2005) to describe the degrees of abrasion herein including: A. showing no surface abrasions, B. showing little surface abrasion, C. showing significant surface abrasion with a smooth surface.

2.3.2.3 Surface Marks

Surface marks are more ambiguous in their origin and manifest as some sort of imprint, scratch, or other trace left by either inanimate objects or a biological agent. Frequently, these include traces from coprophagous invertebrates as surface scratches or burrows (Northwood, 2005). A few samples show plausible evidence of invertebrate scratch marks, displayed as short, radiating, unbranching scratches with no unified orientation can be seen (Fig. 2.3B). Whether these markings are biogenic or abiogenic (i.e., abrasion) is difficult to decern with any confidence. Notably, the scale of these marks is comparable to the surface expression of exposed hair molds (i.e., RAM 17403 and 17557), which appear as fine linear impressions on the coprolites' surface (Fig. 2.3C). Two specimens (RAM17540 and 31212) show evidence of burrowing, in the form of

clustered circular holes of approximately equal diameter (Fig. 2.3D) that cannot be attributed to hair molds or cancellous bone structure.

2.3.2.4 *Breakage and compaction*

Breakage in coprolite samples is any sort of mark that shows that the sample has broken after the fossilization process. Breakages are more likely to occur close to surface inclusions within the coprolite (Northwood, 2005), which tend to cause weak points on the surface (Northwood, 2005). The extent of breakage within the present dataset varies from small portions of the coprolite chipped off (Fig. 2.2H, I, K) to large portions of the coprolite volume presumably missing (i.e., RAM 17546; Fig. 2.2E). The angularity and roughness of the fractured surface also inform residence time since the breakage was made. Some of the coprolite specimens show partially smoothed fracture surfaces, such as RAM 18171 (Fig. 2.2A), indicative of subsequent weathering compared to the fresher fractures in other specimens such as RAM 17547 (Fig. 2.2E). There is limited evidence of post-lithification compaction, with only a single specimen displaying compound fracture on the surface (Fig. 2.3E).

2.3.2.5 *Decomposition and distortion*

Decomposition of the feces prior to lithification is the main cause of spherical to irregular cavities on the coprolite surfaces (Northwood, 2005). Such features were present in both Class I and Class II coprolites and varied in size from submillimetric scales to spanning several millimeters across. The Class I coprolites have larger surface pores which are best preserved in RAM 17546 and 17370 (Fig. 2.2F and G respectively). The surface cavities were described based on their relative abundance and the results are summarized in Table

2. One notable cavity was a linear feature with closely spaced repeated circular depressions (Fig. 2.3F). Though this may be related to gaseous trapping, it may also represent the former mold of a surface inclusion or even trace from a coprophagous vertebrate. Several coprolite samples also display a ventrally flattened surface associated with prefossilization plasticity of the sample. This feature provides some indication of the moisture content of the original scat when excreted and tends to be more characteristic of the larger Class I coprolite samples.

Table 2. Summary of the surface taphonomic features observed in each of the samples investigated in this study. Categories used for abrasions include A= showing no surface abrasion; B= showing little abrasions; C= showing significant abrasions.

Class	Sample Name	Desiccation	Abrasions	Surface Marks	Adhesion	Burrows	Decomposition	Breakage	Compaction
Class I	RAM 18171	Yes	C	No	No	No	None to Little	No	Yes
Class I	RAM 17517	Yes	B	Yes	Yes	No	None to Little	Yes	No
Class I	RAM 17540	Yes	C	Yes	Yes	Yes	Small and Large Pores	No	No
Class I	RAM 17405	No	C	No	Yes	No	Small Pores	Yes	No
Class I	RAM 17547	Yes	C	No	Yes	No	Small Pores	Yes	Yes
Class I	RAM 17546	Yes	B	Yes	Yes	No	Small and Large Pores	No	No
Class I	RAM 17370	Yes	A	No	No	No	Small and Large Pores	No	No
Class II	RAM 17557	No	C	No	No	No	None to Little	Yes	No
Class II	RAM 31214	No	C	No	No	No	Small Pores	No	No
Class II	RAM 31212	No	C	No	Yes	Yes	Small Pores	No	No
Class II	RAM 31211	No	C	No	Yes	No	Pit Marks	No	No
Class II	RAM 31209	No	A-B	No	No	No	Pit Marks	No	No

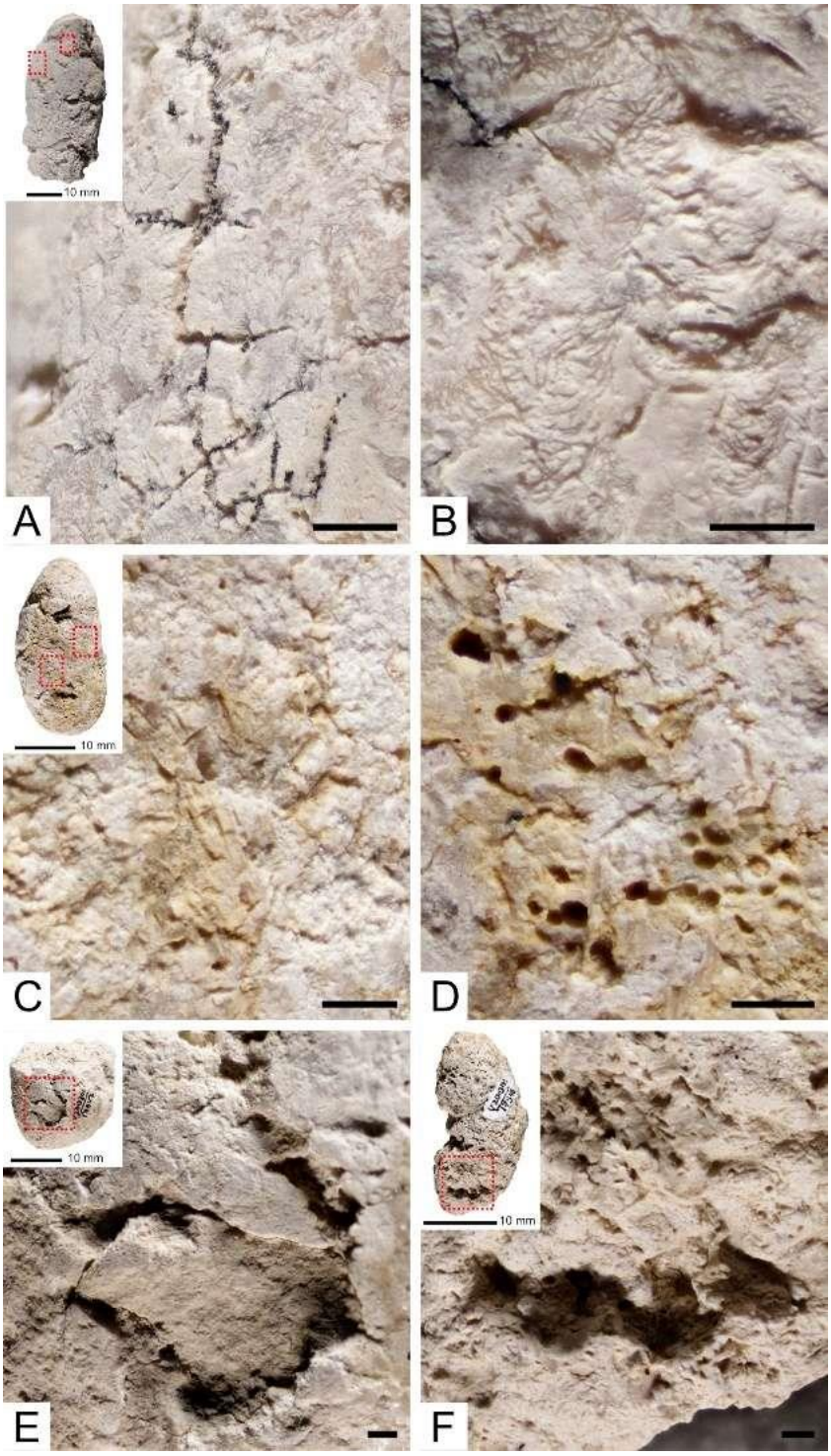

Figure 2.3. A. Examples of small desiccation cracks on the coprolites surface (RAM 17517). **B.** Shows the surface scratches that have no consistent length or pattern to them. **C.** Hair molds seen on the surface of RAM 17540. Very straight and deeper appearance compared to the surface scratches. **D.** Surface borrows seen on RAM 17540. **E.** Post

fossilization fracture seen on the surface of RAM 17547. **F.** Large surface pore seen on RAM 17546. Scale bars represent 1 mm unless otherwise stated.

2.3.3 *Coprolite internal morphology and inclusions*

X-ray microscopy reveals several internal constituents within the matrix of sampled coprolites, including pores, bone inclusions, and even moldic remains of fossil hair. Moreover, segmentation of pore space revealed two distinct types, including more open irregularly shaped pores and a separate group of thin linear structures. Identification of the latter was further verified using light microscopy and SEM, which revealed these structures as the preserved moldic remains of fossil hair. Details of the respective internal components is provided below.

2.3.3.1 Matrix

Petrographic analysis reveals the coprolite matrix as very-fine to medium-grained composition that is predominantly amorphous phosphate though small indistinguishable bone fragments also make up much of the groundmass. There is some evidence of digestive corrosion surfaces and enrichment along defined boundaries within the coprolite (Fig. 2.4A), though sometimes the distinction between different compositional textures is more diffuse (Fig. 2.4B). SEM and EDS analysis of RAM 17546 confirms much of the coprolite matrix is composed of calcium and phosphorous (fluorapatite), with minor traces of silicon, aluminum, and iron (Figs. 2.5 and 2.6). X-ray microscopy reveals a mostly homogenous matrix with some discrepancies in the greyscale values owing to compositional and density differences between the bones and amorphous coprolite matrix. The latter facilitated 3D segmentation as the matrix could be distinguished from the bone inclusions by adjusting the greyscale threshold range. Select

parts of the external surface of the coprolite exhibit visible delineations between the fluorapatite matrix and adhered sediment (Fig. 2.4E) as revealed by enrichment in aluminum and potassium (Fig. 2.6B). Iron was present dispersed throughout the matrix and occasionally concentrated closer towards the pores in the coprolite (Fig. 2.6). Petrographic and SEM analysis show further evidence of desiccation cracks extending inwards from the surface of the coprolite.

2.3.3.2 Pores

Pores were one of the major structural elements within the coprolites, ranging in volume between 0.05–2.72 mm^3, and feret distances of 0.196–19.674 mm. There were no universal pore shapes, ranging from long and thin to large and irregular in shape (Figs 2.4C–D. 2.7, and 2.8). Light microscopy and SEM analysis of RAM 17540 reveal the pores within the coprolite are frequently lined with crusts of botryoidal silica (Fig. 2.4C–D, 2.6C–D). Pores would often connect to one another, affecting the overall shape of the pores, but the majority were isolated from the surface (Fig. 2.8). Their respective proportion within the coprolite volume was the second largest constituent after the matrix, comprising between 3.8–21.1% of the coprolite volume across both size classes (Fig. 2.8). The number of pores per specimen varied and appears to have been influenced by the relative proportion of bone inclusions within the matrix. Though notably, except for one coprolite (specimen RAM 31211), the pores made up more of the coprolite compared to the bones within the matrix (Fig. 2.8J).

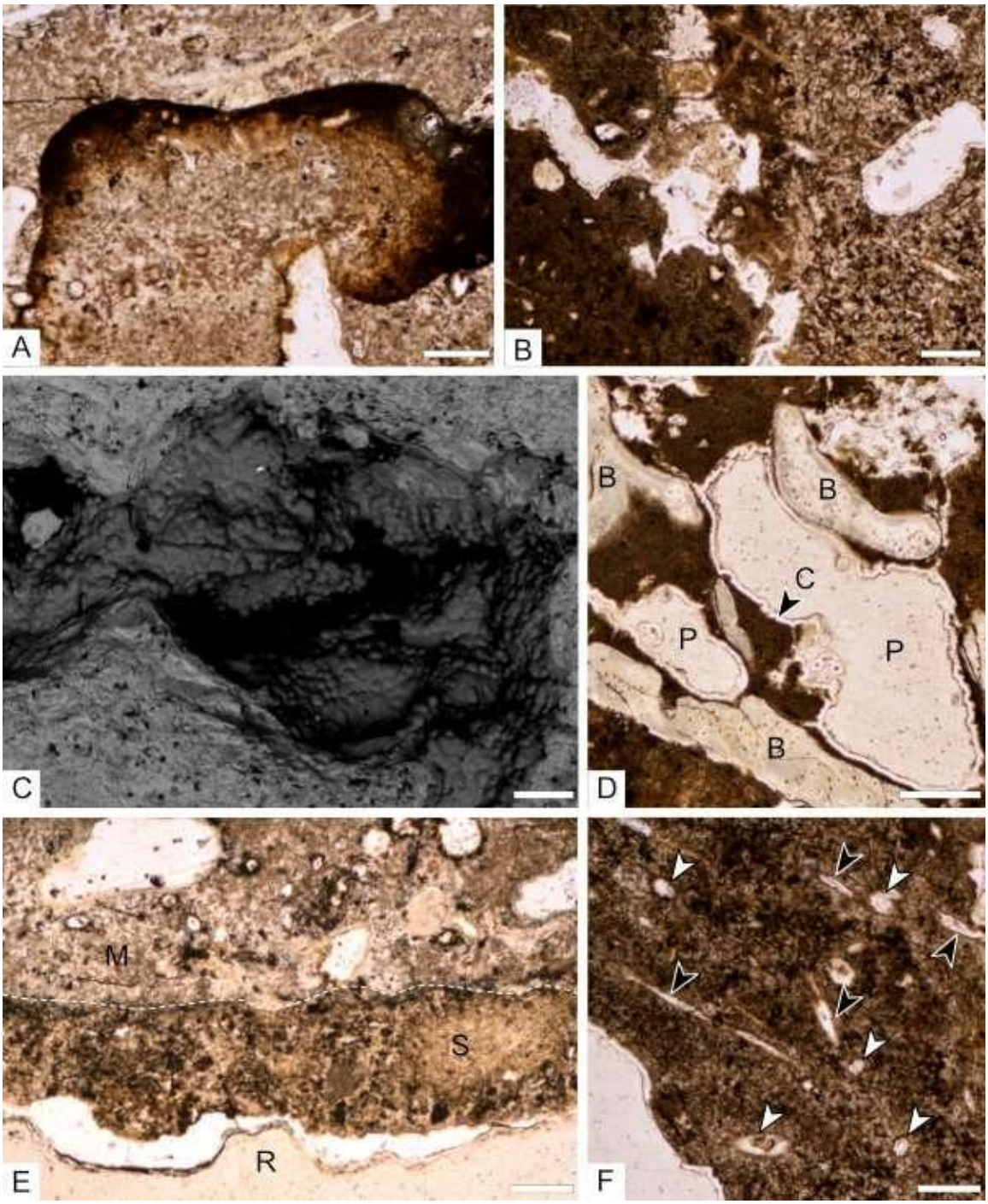

Figure 2.4. Photomicrographs and backscattered electron images of interior composition of specimen RAM 17546. **A.** Phosphate enriched inclusion embedded within matrix of coprolite. **B.** Contact between two fabrics of matrix in the interior of the coprolite**. C.** Backscattered electron image of three-dimensional pore space showing botryoidal silica crust. **D.** Pore spaces lined with silica crust and bone inclusions**. E.** Contact between coprolite matrix and adhered layer of sediment**. F.** Transverse (white arrows) and longitudinal (black arrows) cross sections of hair molds. B= bone; P=pore; C=crust; M=matrix; S=sediment; R=resin. Scale bars represent 250µm.

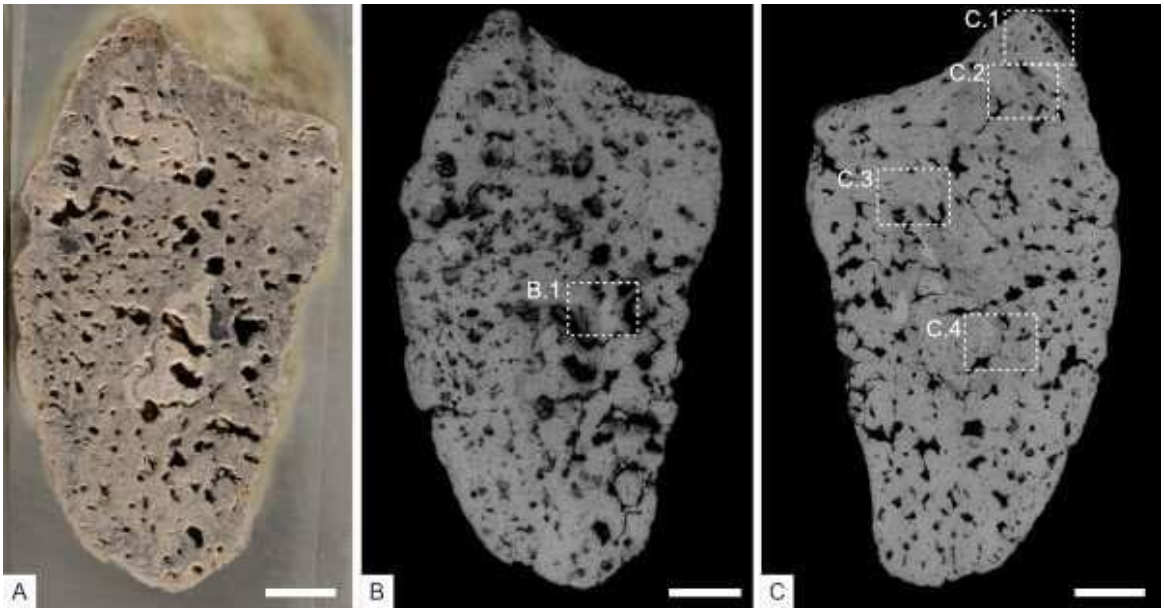

Figure 2.5. A. Plane view of the unpolished sectioned surface of RAM 17546 under plain light. **B.** Backscatter electron image of the same surface figured in A**. C.** Back-scatter electron image of polished surface of sectioned sample. Scale bars represent 5 mm.

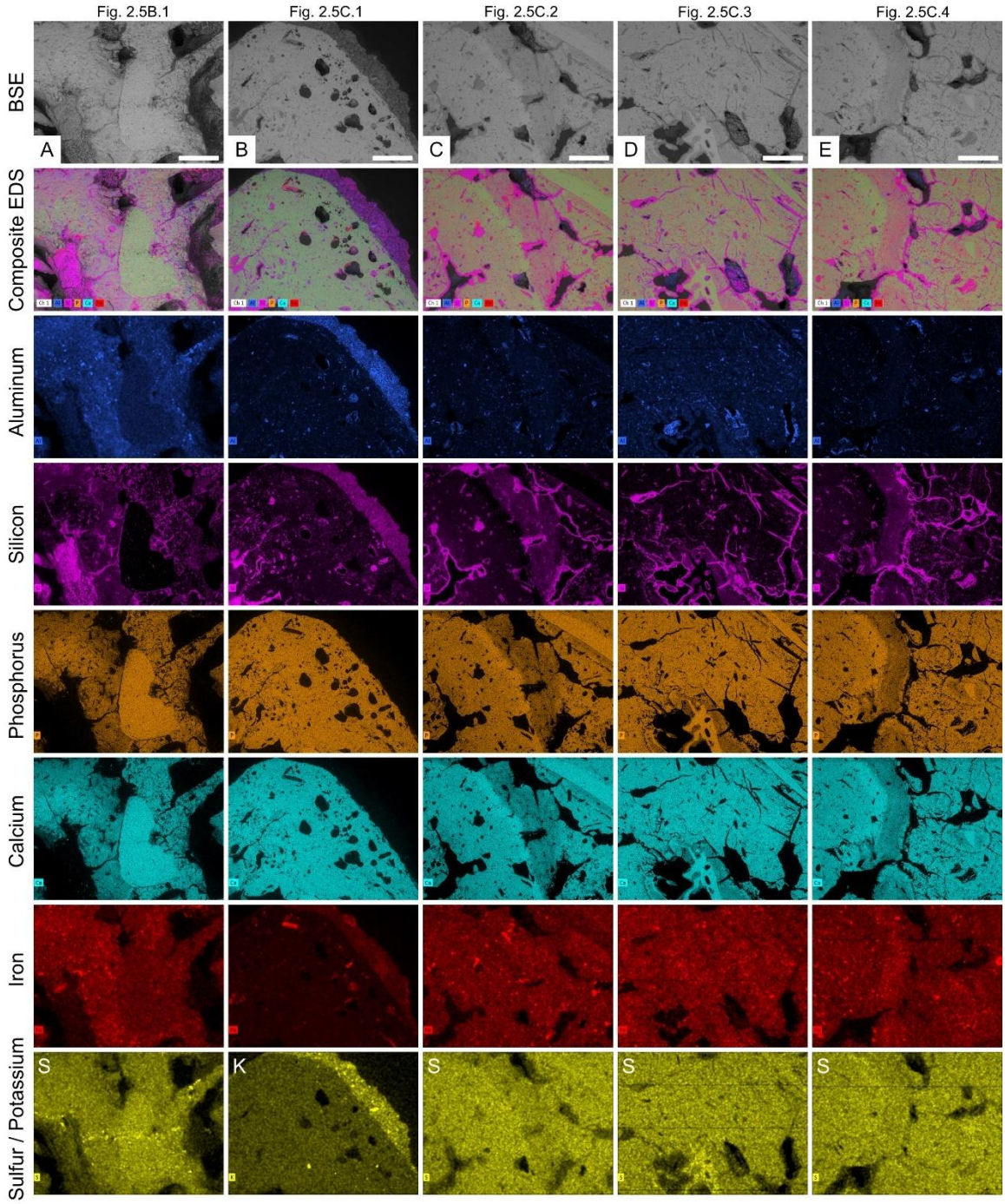

Figure 2.6. EDS elemental maps of areas in specimen RAM 17546 from Fig. 2.5. **A**. Well-preserved bone inclusion and surrounding matrix. **B.** Exterior edge of the coprolite showing sediment adhered to the outer surface. **C.** Etched bone inclusions with diffuse edges. **D**. Matrix and hair molds. **E**. Etched bone inclusions with diffuse edges. Scale bars represent 1 mm.

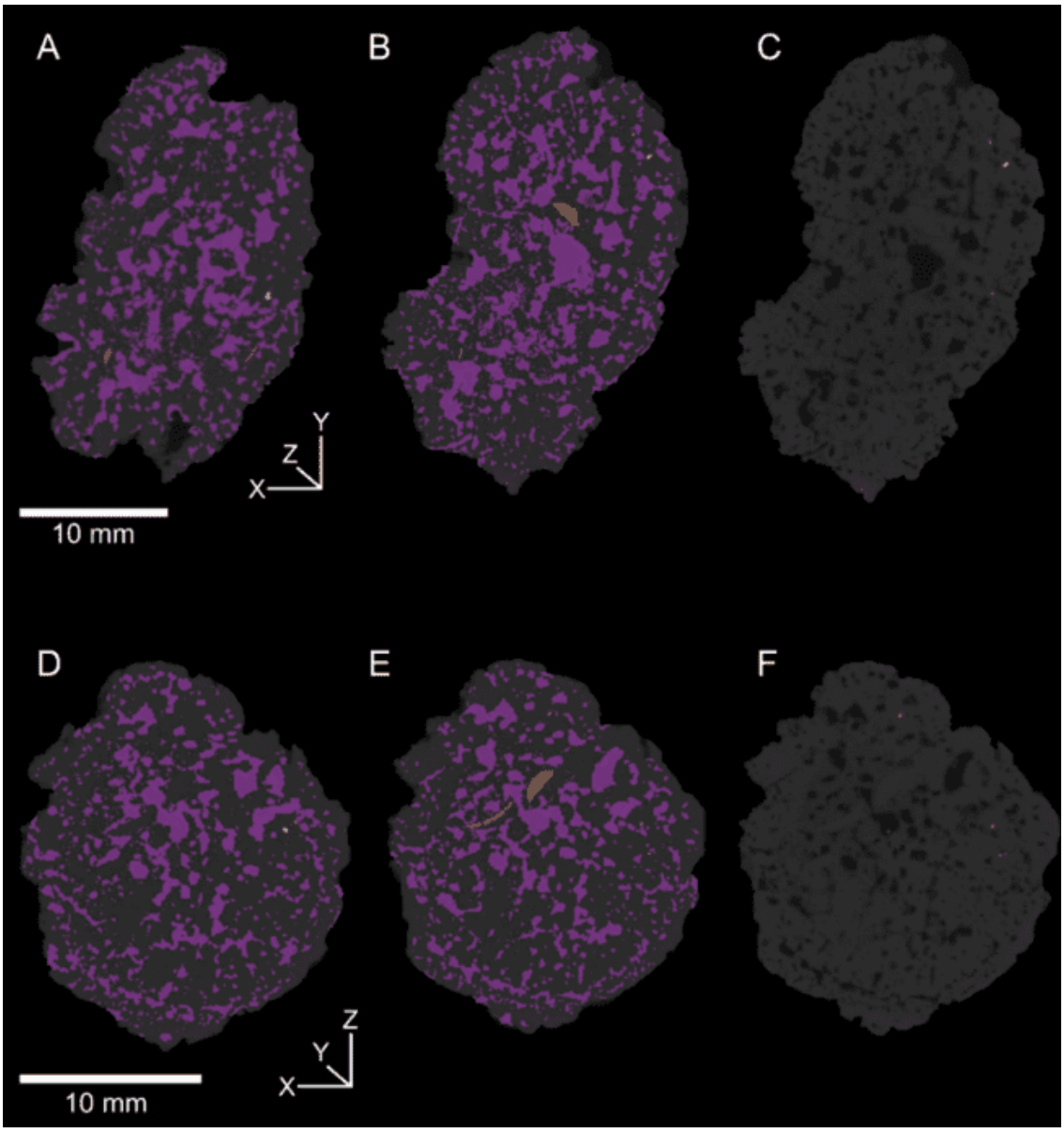

Figure 2.7. Tomographic projections of RAM 17546 taken from two different cross-sections. **A–C.** Longitudinal cross-section **A.** Only showing pores (purple). **B. S**howing both pores (purple) and bone (orange). **C.** Showing tomographic slice B without segments highlighted. **D–F.** Transverse cross-section. **D.** Only showing pores (purple). **E.** Showing both pores (purple) and bone (orange). **F.** Showing tomographic slice of E without segments highlighted.

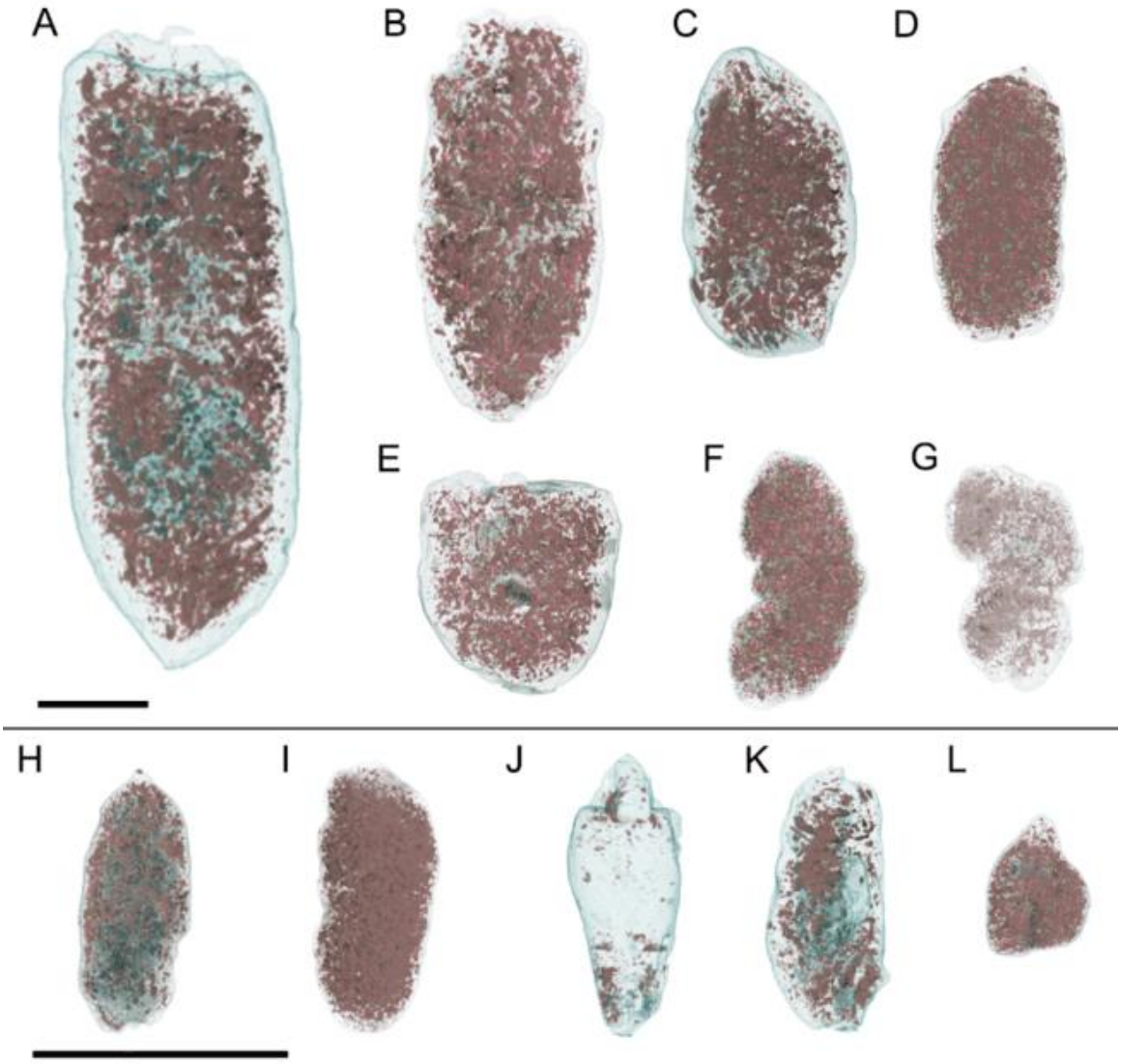

Figure 2.8. Internal view of pores of Class I Coprolites (A–G) and Class II (H–J). Pores are colored in in brown while the outside of the coprolite is represented by light blue. Scale bars represent 10 mm.

2.3.3.3 Hair inclusions

Among the notable features detected using µCT were µm-scale structures that represent the moldic remains of fossil hair within the coprolite matrix. Unlike the pore spaces or other taphonomic features, these structures had a distinct morphology that did not exhibit random branching (e.g., desiccation cracks). The hair filaments are present as elongated, fine lines with circular cross-sections that are easily discernable in thin section (Fig.

2.4F). Like the pores in the coprolite, these molds were infilled with silicon (Fig. 2.6D). Fossilized hair structures were also pronounced in tomographic projections of specimen RAM 17540, which was rescanned targeting a specific region to examine the hair constituent in detail (Fig. 2.9). The resultant high-resolution scan revealed the small elongate, tube-like structures, each only lasting a few slices. Molds were distributed relatively evenly throughout the scanned ~1cm core (Fig. 2.9), however, the distribution of the hair throughout the entire coprolite showed more variability.

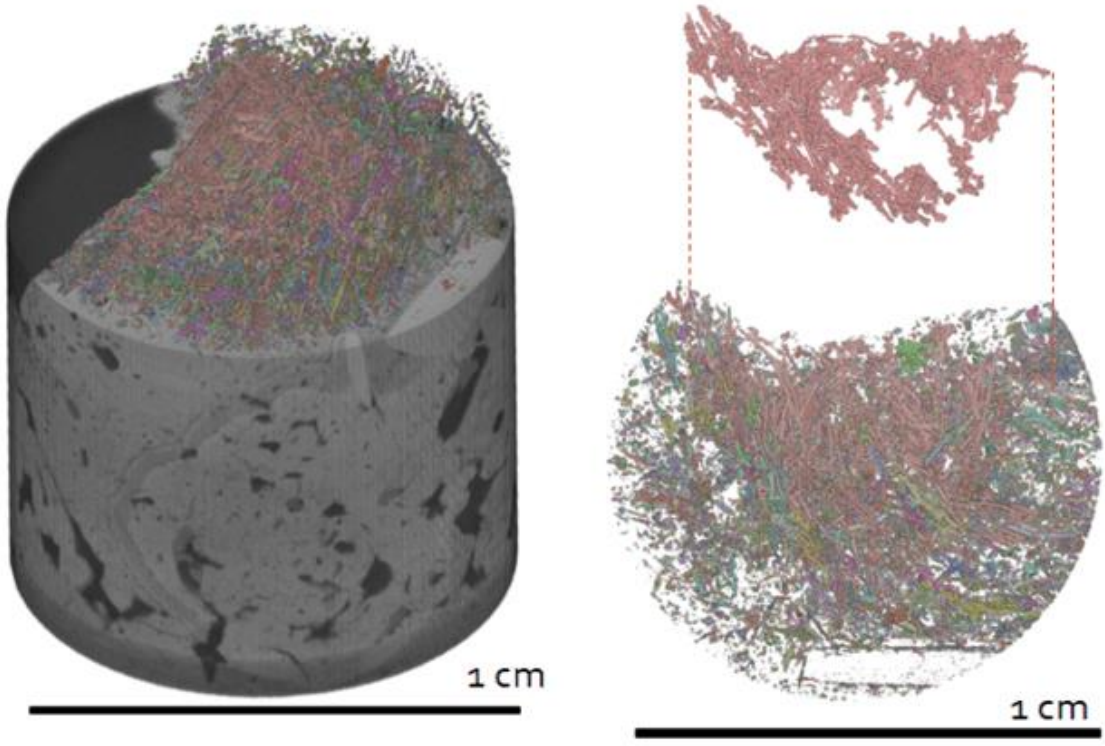

Figure 2.9. High resolution scans of RAM 17540. Highlighted within the scan are tube like structures identified as hair structures preserved within the coprolite.

2.3.4 *Bone inclusions*

Bone inclusions visible on the exterior of the coprolites were often dark in color relative to the surrounding matrix. The sectioned surface and corresponding thin section of RAM

17540 reveals that bone inclusions varied in their quality of preservation, ranging from better preserved fragments (i.e., dark with clear external surfaces) to heavily corroded and poorly preserved bone material (i.e., buff-colored with ill-defined margins) (Fig. 2.5A; compare Fig. 2.6A [well-preserved] with Fig. 2.6E [poorly preserved]). SEM-EDS shows a thin layer of silicon, calcium, and phosphorus formed around the outer surface of the bone (Fig. 2.14). Using SEM, phosphorus and calcium could be seen around the bone. Segmentation of the μCT data shows a considerable variation in the size and degree of fragmentation of bone inclusions, with a maximum bone feret diameter of 16.56 mm for the Class I coprolites and 25.73mm for Class II. Except for a few coprolites, principally those preserving parts of long bones (inc. RAM18171, Fig. 2.10A; RAM 17557, Fig. 2.10H; RAM31212, Fig. 2.10J), there is limited evidence of preferred bone orientation due to the overly fragmented nature of the inclusions. More typically, smaller bone fragments are visible ‘floating’ around the larger bones within the groundmass of the coprolite.

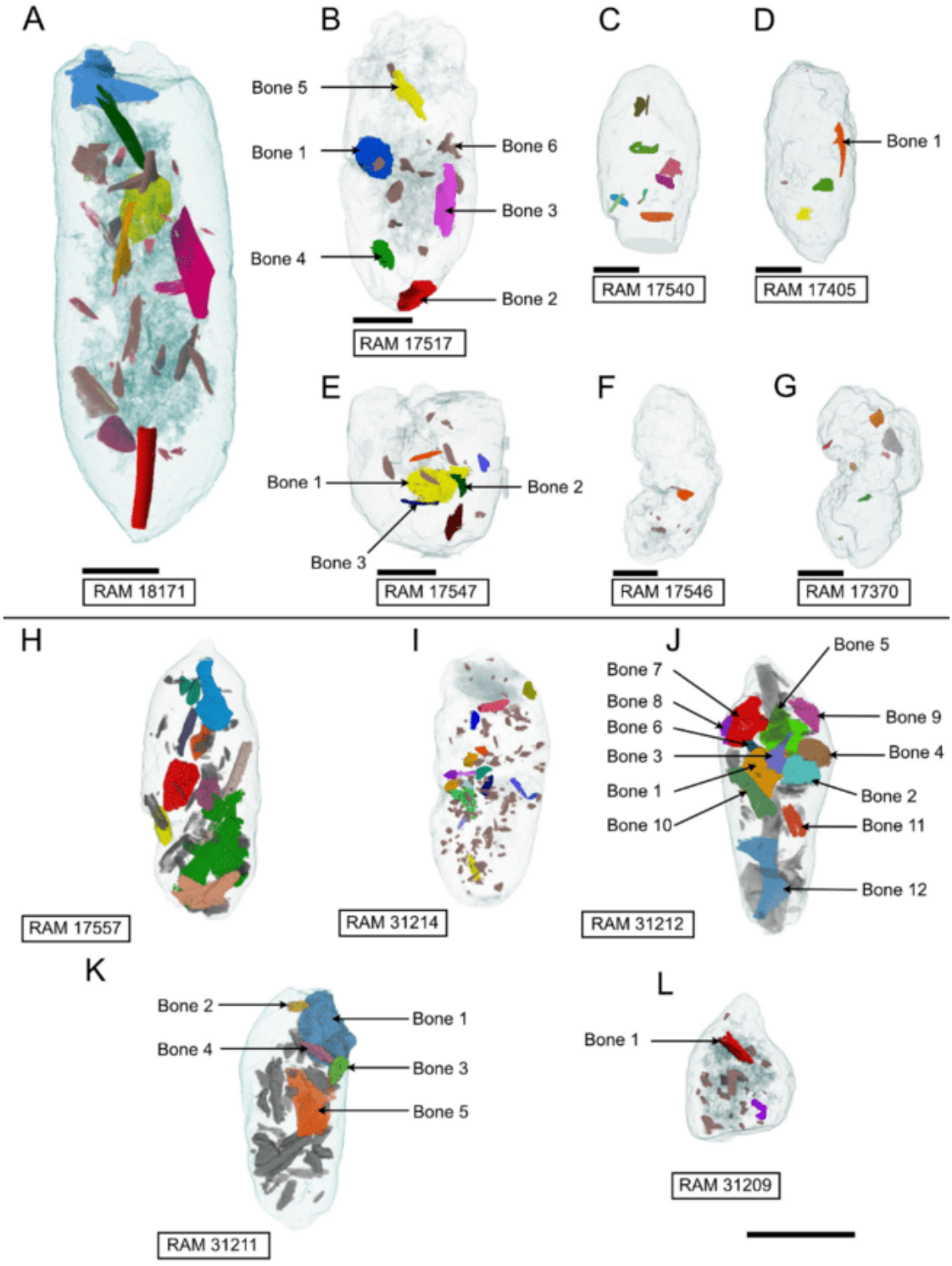

Figure 2.10. Internal view of coprolite bone inclusions divided into size Class I (A-G) and Class II (H-L). Bones of interest labeled. Scale bars 10mm.

A total of 437 bones were virtually extracted from the 12 coprolites examined. Due to their predominantly fragmentary nature (most smaller than $1mm^3$) the majority could not be identified to any single taxon. However, a select few segmented bones preserve sufficient morphological detail outside of just the general shape to allow attribution to a particular anatomical bone type.

2.3.4.1 Bones with recognizable features

RAM 31212, Bone 1 (Fig. 2.11A): this bone is fragmented at the distal end, though the proximal morphology remains well preserved with a clear rounded head and portion of the neck indicative of a ball joint in a femur or humerus. This represents the largest individual bone inclusion by volume in this coprolite and most likely belonged to a small mammal.

RAM 31212, Bone 3 (Fig. 2.11B): though incomplete, this bone is characterized by an elongate and narrow process projecting from a sub-triangular flattened face. From the side profile, a small triangular bump is pronounced towards the base of the bone in the figured orientation. The bone then extends outwards from this flat face at approximately a right angle to the narrow process, until the rest of the bone is broken. Significant etching from digestion can be seen on the bone, most obviously on the irregular broken surface where the cancellous structure is exposed. Identification is made difficult by the incompleteness of the bone but may resemble a part of a zygomatic arch of a small mammal.

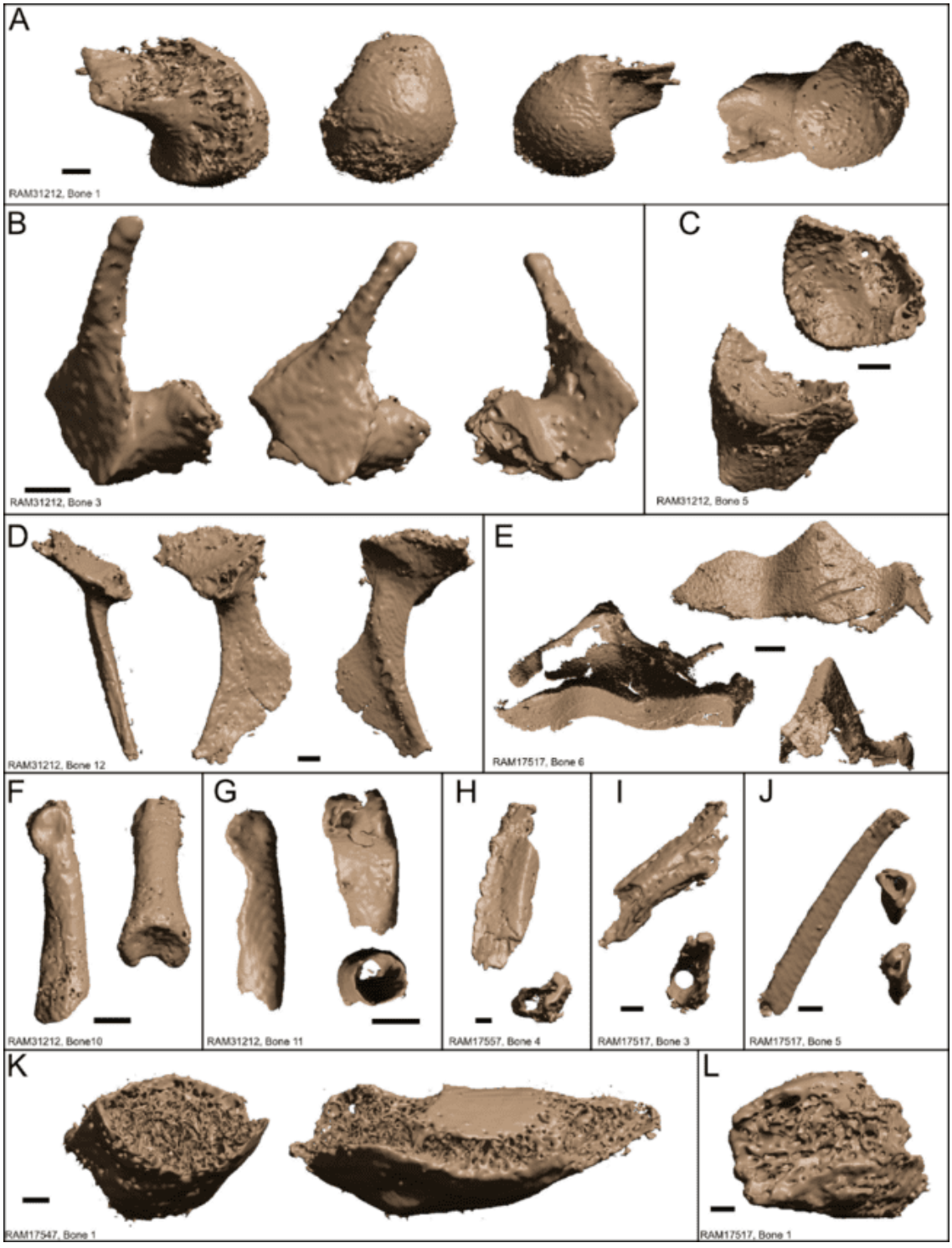

Figure 2.11. A: Bone 1 of RAM 31212 seen from four different angles. Shows the rounded joint part of the bone and the decay of the bone. **B:** Bone 2 of RAM 17517 seen from three angles showing the zygomatic arch. **C:** Bone 5 of RAM 31212 seen from two angles, showing acetabulum (socket) of a pelvis bone. **D**: Bone 12 of RAM 31212 seen from three different angles, showing a potential pubic bone related to C. **E:** 'Bone 6' of

RAM 17517 seen from three angles. This bone is potentially not mammal material. **F:** Bone 10 of RAM 31212 seen from two views. Bone identified as a phalange. **G:** Bone 11 RAM 31212 of RAM 31212 seen from two views. Bone identified as a phalange. **H-I:** Bone 4 of RAM 17557 and Bone 3 of RAM 17517 each from two views. Both are flat, short bones that are hollow. **J:** Bone 5 of RAM 17517 seen in two views. A long flat bone with a hollow center throughout. **K-L:** Bone 1 of RAM 17547 and Bone 1 of 17517 show the cancellous structures of the bones contained within the interior. Scale bars represent 1 mm.

RAM 31212, Bone 5 (Fig. 2.11C): this bone features a large, circular concave depression that can be identified as some sort of socket. It is likely an acetabulum (socket) of an innominate bone (pelvis). The dimensions are comparable in size to the head of RAM 31212 Bone 1 and therefore the two may have been associated in vivo.

RAM31212, Bone 12 (Fig. 2.11D): Due to the bone's location in RAM 31212, there is a possibility that this bone is a pubic bone associated with Bone 5 (Fig 2.11C). It is mostly flat with a ridge-like structure on one of the sides of the bone. The top of the bone features what appears to be some sort of connective point to another bone.

RAM17517, Bone 6 (Fig. 2.11E): This bone or structure does not appear to be mammalian. The structure is elongate, sub-triangular in plane view and triangular in frontal view, with two distinct points along the length of a central ridge. While there is no unambiguous identification possible, this may resemble reptilian material, for instance dermal plates. Reptilian remains (i.e., lizard osteoderms) have been found in a previous study of these coprolites (Lofgren et al. 2017).

2.3.4.2 Long and short bones

Several examples of long bones were identified across the coprolite class sizes (Fig. 2.11F–J). These tend to be characterized by a cylindrical elongate shape with a hollow

center where the bone marrow is contained. A few inclusions preserve the proximal or distal ends of the bone, whereas the vast majority of these are preserved as broken fragments which precluded confident identification to any specific anatomical bone (Fig. 2.11K and L). Exceptions to this include bones 10 (phalange) and 11 (phalange) from RAM31212 (Fig 2.11F and G), which in the case of the former is complete and well preserved, measuring 6.3 mm in length and 1.2 mm in width. Select fragments, including Bone 4 of RAM 17557 and Bone 3 of RAM 17517 do exhibit a slight ridge along one side of the diaphysis. Bone 5 of RAM 17517 also exhibits a sub-triangular cross section with slight tapper in thickness along its sagittal length which might suggest this is a portion of a rib bone (in which case this would be considered a flat bone). The lack of preserved cancellous bone in the proximal and distal ephiphysis of the fragmented limb bones suggested these finer spongy textures were prone to dissolution via digestive processes.

2.3.4.3 Cancellous Bones

Often the largest bone inclusions are irregularly shaped fragments of cancellous bone which are characterized by a network of spongy tissue called trabeculae (Fig. 2.11K and L). Though this porous bone is typical of vertebral bones and the articulating ends of long bones, the extremely fragmented nature of the specimens herein once again precludes any confident identification. Examples of these occur across the bone size classes, including Bone 1 in RAM 17547 (Fig. 2.11K), and 17517 (Fig. 2.11L). Common features associated with these fragments include varying extents of decay and digestion as indicated by the varying thickness of the trabeculae.

2.3.4.4 Flat bones

These bones are typically thin and flat, possibly with some minor curvature and are composed of compact bone occasionally separated by a thin layer of cancellous bone. Fragmentation and digestion make it impossible to make any sort of reliable identification, however, by definition, these are affiliated with parts of the cranium, sternum, ribs, and scapulae. Despite their poor preservation, certain attributes show evidence of mastication and feeding behavior. For instance, Bone 1 in RAM 31209 (Fig. 2.12A) displays two layers of flattened bone where one layer has been partly crushed while the other remains intact. Because this has not impacted the entire bone fragment, it indicates that this breakage does not stem from just digestion or decay of the bone. Other examples of flattened bone fragments vary in thickness and shape. Bone 5 in RAM 31209 (Fig. 2.12B) is extremely thin, with one face relatively smooth while the other exhibits a few randomly distributed bumps. The thickness of the bone alone suggests this is most likely cranial in origin. In plane view, Bone 1 in RAM 17405 (Fig. 2.12A) possesses an elongated structure with slight curvature along the sagittal length, and a rounded base and flat top. In frontal view, one side of the bone (Fig. 2.12D) predominantly smooth while the other displays two distinct ridges with a curved depression between them. Even though the structure does not appear to be complete, the curvature is clear and could indicate some type of articulation structure. Bone 1 in RAM 18171 (Fig. 2.12D) features a comparable semicircular shape between two distinct ridges and a flattened opposite surface. Other fragments that bear a close similarity to one another include Bones 1 and 3 in RAM 31214. Both these bones show evidence of two adjacent yet separate thin layers of compact bone. One side is notably postmarked by small circular holes that open to the

secondary bone layer below. Whilst the opposite outer surface of the bone features small circular, evenly convex bumps regularly distributed across the surface. Despite these defining features it is difficult to attribute these bones to any particular structure. Several smaller portions of flat bone are common within the coprolites, often exhibiting sub-triangular outlines, for instance, Bone 1 in RAM 17370 (Fig. 2.12H) and Bone 2 in RAM 18171 (Fig. 2.12G). In both these instances, the bones possess a slight concavity on one side of the bone and a gentle curvature to the overall shape of the bone. The depression may not continue along the length of the bone and instead tappers and pinches out along one edge (Figure. 2.12G–H). This could give some indication that the bone might have been part of a larger bone that was broken. Identification is not possible as there are no clear marks that could indicate what bone this might have been.

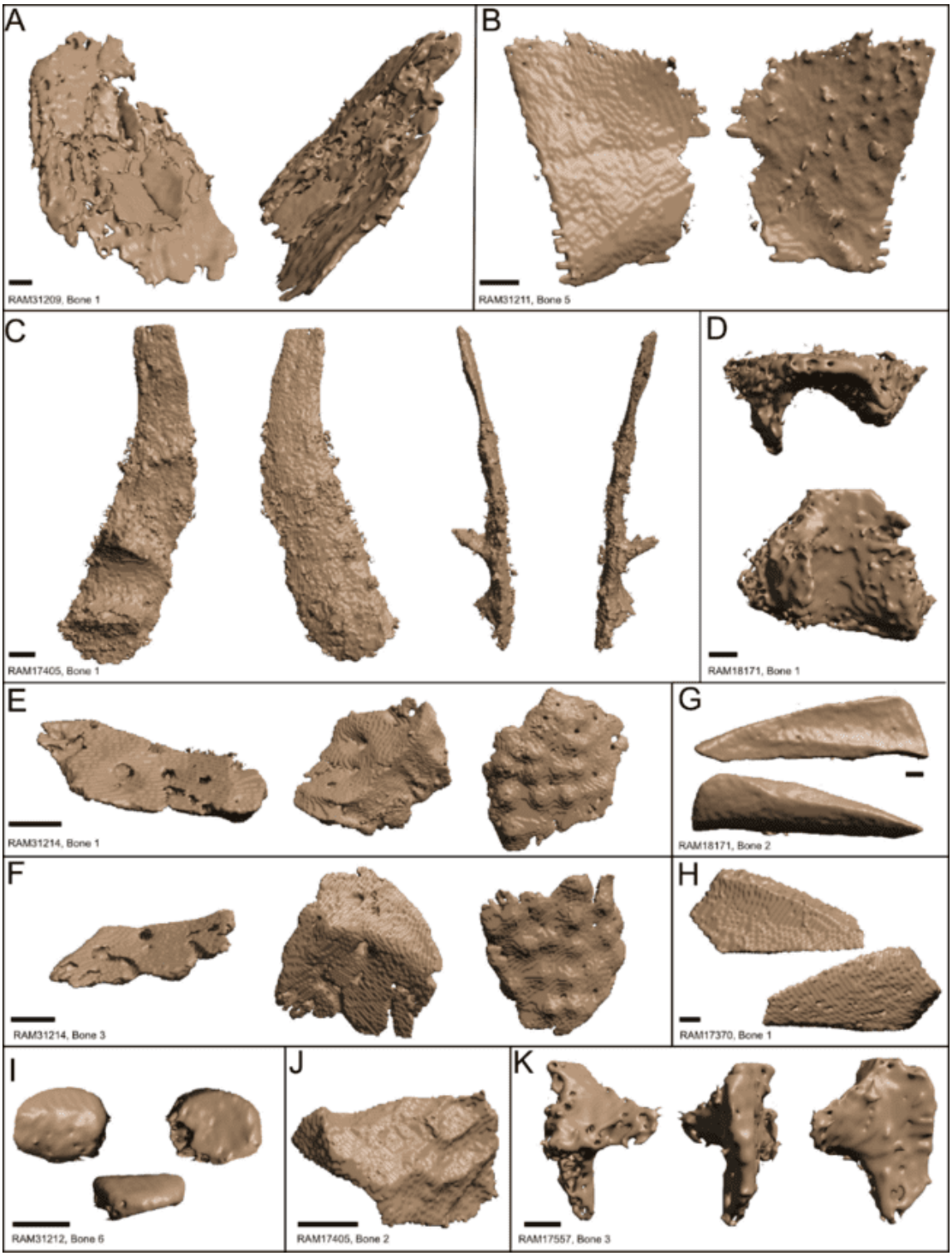

Figure 2.12. A-H. Flat bones. **A.** Plane and oblique view of Bone 1 in RAM 31209. **B**. Plan views of opposite sides to Bone 5 in RAM 31209. **C.** Plane and side views of Bone 1 of RAM 17405. **D.** Plane and side views of Bone 1 in RAM 18171. **E.** Oblique and plane views of opposite sides to Bone 1 in RAM 31214. **F.** Oblique and plane views of opposite sides to Bone 3 in RAM 31214. **G.** Opposing flattened sides of Bone 2 in RAM

18171. H. Opposing flattened sides in Bone 1 of RAM 17370. **I-K.** Irregular bones. **I.** Patella in anterior, lateral, and posterior views. **J.** Plane view of Bone 2 of RAM 17405. **K.** Plane and side views of Bone 3 of RAM 17557. Scale bars represent 1mm.

2.3.4.5 Irregular bones

Irregular bones encompass those that vary considerably in shape and structure to the other bone types and include sesamoid bones (i.e., those embedded in tendons) as well as vertebrae and bones of the pelvis. Besides those that have already been described in section 2.4.4.1, bone 6 in RAM31212 (Fig. 2.12I) can be identified as a likely patella, with sub-circular outline and flattened articular surface that would have sat adjacent to the medial condyle of the femur. Remaining irregular bone fragments cannot be confidently attributed to single anatomical bone. Bone 2 in RAM 17405 has a predominant curved plate-like shape with an irregular surface, including small concavities on the right-hand side of the sample as shown in Figure 2.17J. The thickness and size of this bone might suggest it is associated with the pelvis, but beyond size there are no reliable indicators of this identification. Bone 3 in RAM 17557 (Fig. 2.12K) also has an irregular shape and sits on top of bone 4. It shows some cancellous bone, but it is not densely packed like other bones of the same texture. There are three dominant ridged edges that can be seen from the top of the bone. Two of these ridges form a triangle-like shape. The other ridge forms a flat face on the side of the bone.

2.3.3 *Results of statistical analyses*

In total 12 coprolites were included in the statistical analysis for determining different classes of coprolites. Three parameters (height, width, and mass) were used to create a

plot (Fig. 2.13A), which visually suggests that there are two distinct classes of coprolites within the sample. Statistical significance was not tested due to the small sample size of coprolites (Class I, n=7; Class II, n=5). Additionally, it was tested to see whether there was a difference between the relative proportions of skeletal inclusions between the two different size classes (Fig. 2.13B). Again, limited sample size and overlap in the distribution of the data precluded meaningful statistical analyses and could not determine between size class using overall proportion of bones within the coprolite sample.

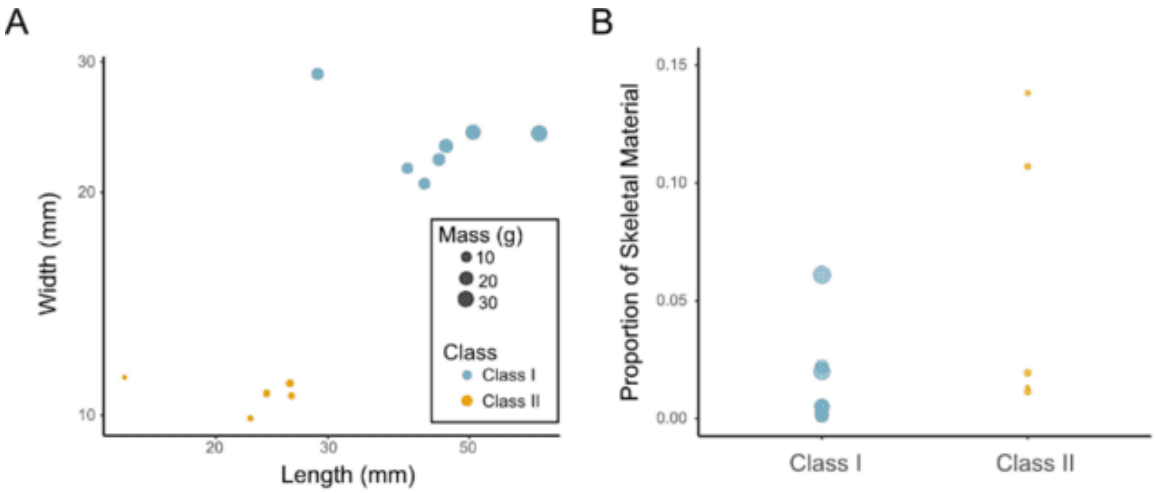

Figure 2.13. A. Shows coprolite on a x-y plot, the coprolite samples plotted length vs width. The size of the dots indicates the mass of the coprolite specimen. Class I coprolites are grouped near the top right of the plot while Class II coprolites are grouped near the bottom middle. **B.** Shows the proportion of skeletal material per coprolite specimen between the two classes.

Volumetric measurements and the relative proportions that selected constituents each contribute to the individual coprolite samples can be seen in Figures 2.14A and B respectively (see also Supplementary Materials Tables 3–5). Excluding specimen RAM 31211, the proportion of pores within the matrix was consistently greater compared to that of bone inclusions (Fig. 2.14B). The lowest percentage of pores in any sample was in RAM 17370, with just under 4%, and the highest percentage at 26.76% in RAM 17546.

Bone inclusions, on the other hand range from 10% in RAM 17546 to 13.82% in RAM 31211, with the latter recording the only time the proportion of bone was greater than that of the pores. Samples RAM 17546 and RAM 17557 exhibit the most pores within a coprolite volume.

Differences in bone size between the two coprolite classes were compared using median values of bone volume, maximum feret diameter, mean feret diameter, and minimum feret diameter (Fig. 2.15A–D). In total 437 bone values were used in the analysis (Class I, N=172; Class II, N=265). There was no significant difference (p=0.1757) between the median bone volumes of Class I (0.1m^3) and Class II (0.1mm^3). The median value of the maximum feret diameters of bones between Class I (1.575 mm) was significantly larger (p=0.001863) than Class II (1.25 mm) via the Wilcoxon test for medians. Similarly, to the maximum feret diameters, there was a significant difference (p=0.0006583) in size between the mean feret diameters of bones of Class I (1.015 mm) and Class II (0.87 mm). The same result can be seen with the minimum feret diameters of bones, with Class I (0.495 mm) significantly larger (p=0.004129) than Class II (0.460 mm).

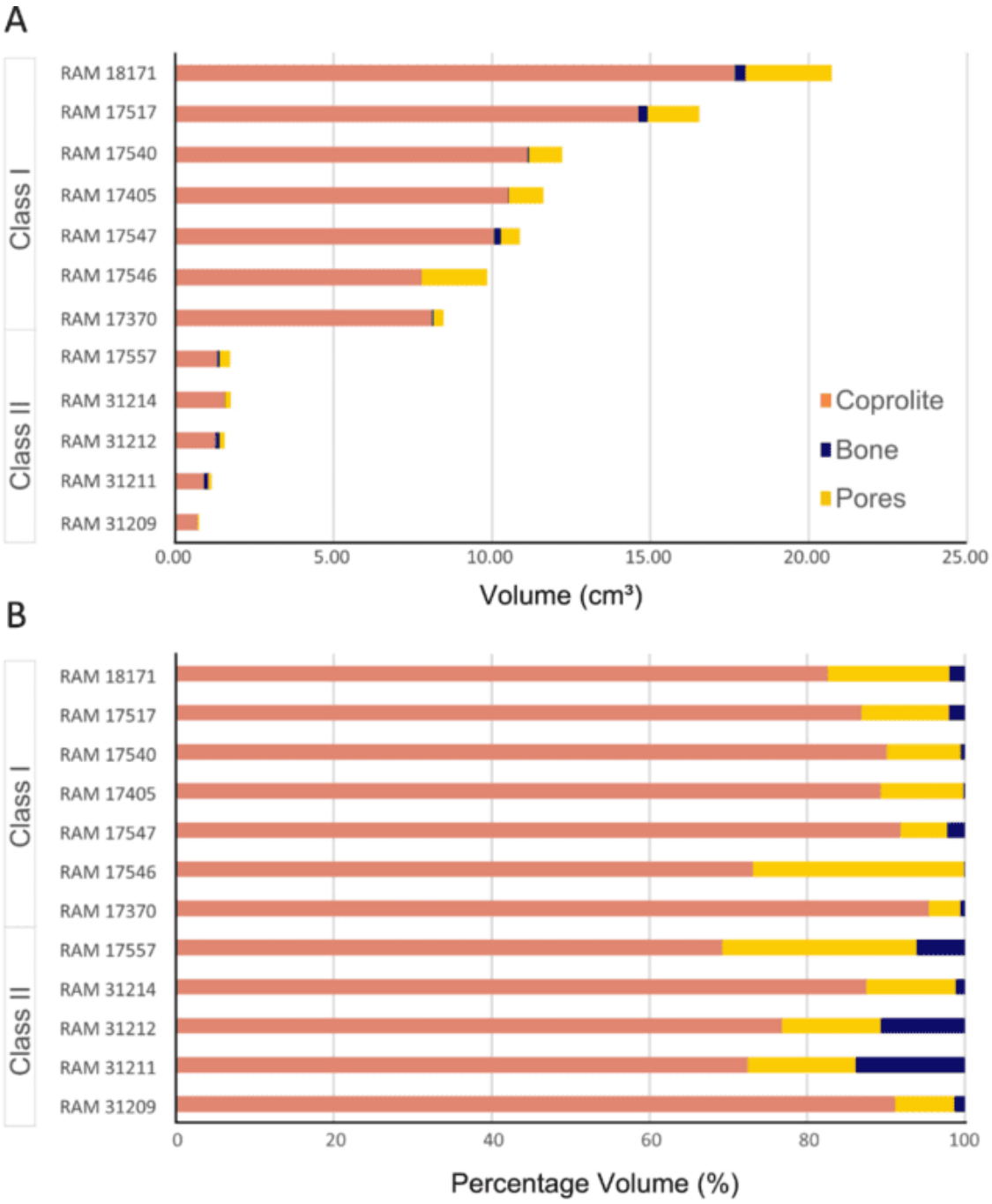

Figure 2.14. **A.** Volumetric analysis of all coprolites, comparing total volume of matrix vs total volume of bones vs total volumes of pores. 1-7 are Class I Coprolites while 8-12 are Class II coprolites. **B.** Volumetric analysis of all coprolites, comparing total percentage of matrix vs total percentage of bones vs total percentage of pores. 1-7 are Class I Coprolites while 8-12 are Class II coprolites.

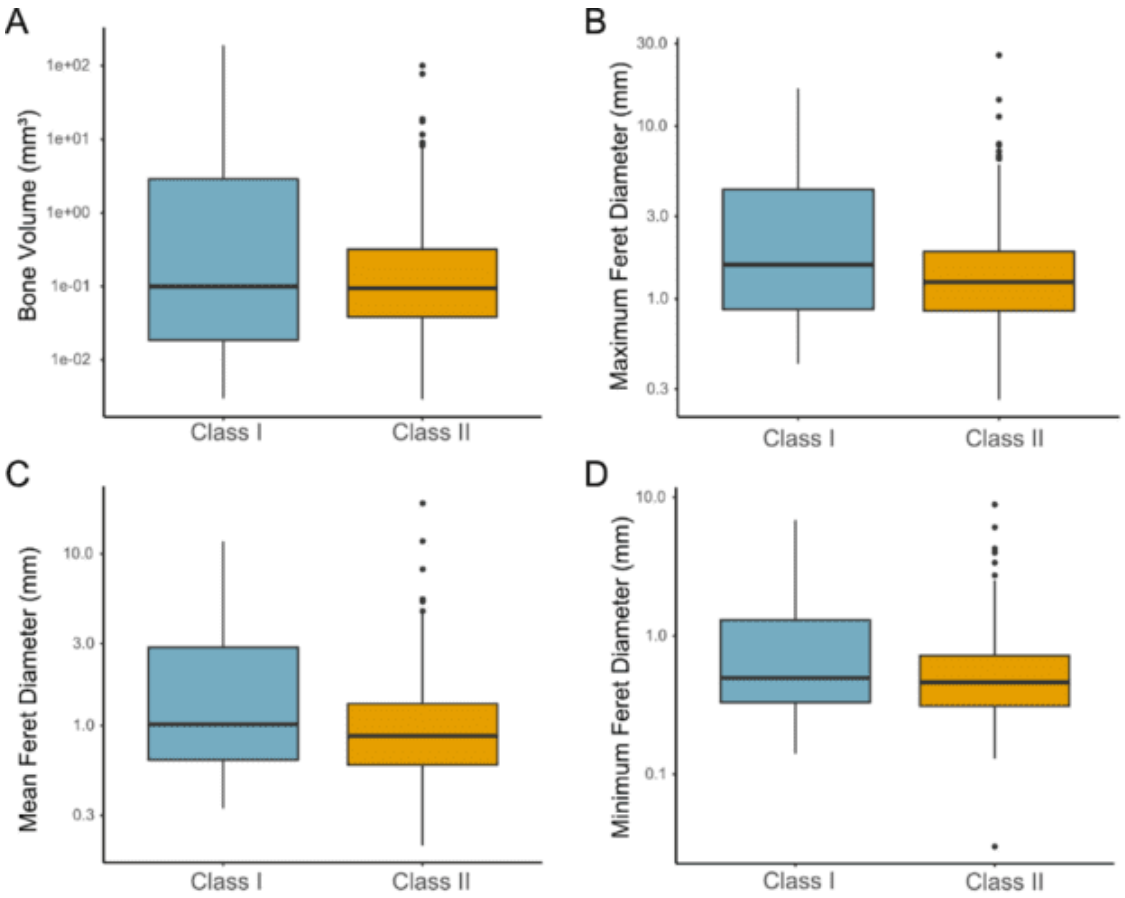

Figure. 2.15. A. Median difference of volumes between Class I (0.1mm^3) and Class II (0.1mm^3). **B.** Median difference between Class I and Class II maximum feret diameters of bones for coprolites (Class I= 1.575 mm, Class II= 1.25 mm, p=0.001863). **C.** Median difference between Class I and Class II mean feret diameters of bones for coprolites (Class I= 1.015 mm, Class II= 0.87 mm, p=0.0006583). **D**. Median difference between Class I and Class II minimum feret diameters of bones for coprolites (Class I= 0.495 mm, Class II= 0.460 mm, p= 0.004129).

2.4 Discussion

2.4.1 *Insights into feeding behavior*

The results of both qualitative and quantitative analyses of the two coprolite size classes reveal some notable differences with respect to the morphology of the inclusions, which may inform about feeding habits and physiological differences in the producers. Though the dataset was too small to reliably discern any statistical difference in the relative

proportions of bone inclusions between Classes I and II, some noteworthy trends emerge. For instance, the proportion of bone volume to total volume was greater in the smaller Class II coprolites by comparison to the Class I coprolites (Fig. 2.15A). Moreover, there was no significant difference in the extracted bone volumes between the two classes indicating that, despite the relative size of the smaller Class II coprolites, the bone constituent was comparable to that observed in larger Class I coprolites.

In the case of Class I coprolites, bones tended to be larger overall with respect to their feret diameters (Fig 2.15B–D). Bone inclusions within the Class I coprolites also showed more degradation and evidence of intense fragmentation, insofar that few could be identified to any particular anatomical bone. This indicates that the Class I producers were capable of consuming larger prey compared to the Class II producers. Bones extracted from the Class I coprolites, including Bone 1 of RAM 17547 (Fig. 2.11K) and Bone 1 of RAM 17517 (Fig. 2.11L), lacked an identifiable shape but revealed internal features such as cancellous structures associated with much larger bones (e.g., pelvic bones, vertebrae, etc.). Given the ambiguous shapes, incomplete condition of the bones and preponderance of homogeneous phosphatic matrix contained within Class I coprolites, this aligns with specific feeding habits and digestive processes. Principally, the evidence presented herein supports a durophagous carnivoran producer with bone crushing habit, which is comparable to previous findings made by Wang et al. (2018) in relation to late Miocene carnivoran coprolites from California. The producers of these latter coprolites are inferred to have been borophagine canids that filled a unique ecological nice in North America, comparable to extant hyenas, until their disappearance approximately 2 million years ago (Lofgren et al 2017; for further discussion see section

2.4.2 below). Like the California specimens, the PSMP coprolites also exhibit a powdered homogenous matrix of bone residues indicative of a producer with a highly acidic gastrointestinal system (Wang et al. 2018). Examples of corrosion are visible in Bone 1 RAM 17547 (Fig. 2.11 K) where internal cancellous bone matrix reveals regions of extremely thin trabecular material. This also accounts for the diffuse boundaries exhibited by several bone inclusions during the segmentation process.

Class II coprolites overall appear to have a larger proportion of bones compared to the total volume of the coprolites, though there is notable variation within the sampled dataset (Fig. 2.13B). This variation is also evident in the condition of extracted inclusions. Most identifiable bones in the PSMP material are associated with specimens in Class II. However, this is slightly skewed as most of these bones were also recovered from a single specimen, RAM 31212 (Fig. 2.10J). This particula coprolite has the second largest amount of bone inclusions (Supplementary Materials, Table 5, 10.70%), with RAM 31211 having the highest overall proportion (Supplementary Materials, Table 5, 13.82%). Three of the Class II coprolites (RAM 31211, 31212 and RAM 17557) are more densely packed with larger bone inclusions suggesting that the producers were capable of consuming the bones whole, with limited mastication of prey items compared to the producers of the Class I coprolites. In this case, producers of these Class II coprolites were able to extract nutrients with little to no bone-crushing required to consume the prey item. Most likely, this is attributed to the size of the prey item itself for which durophagous mastication was not necessary (Pokines and Tersigni-Tarrant, 2012).

The Class II producers also consumed smaller bones compared to Class I producers, as seen by the significantly smaller median values in feret diameters in Class

II compared to Class I (Fig. 2.15 B-D). Notably, these smaller bones show evidence of intense fragmentation, decay, or damage of some sort, as observed in the remaining Class II coprolites (RAM 31209, Fig. 2.10I and 31214; Fig. 2.10L). This observation tends to further support a capacity for bone-crushing when required for larger prey items, or once the higher return nutrient-rich organs had been eaten (Pokines and Tersigni-Tarrant, 2012). More direct evidence for a bone-crushing habit is displayed in Bone 1 of RAM 31209 (Fig. 2.12A) which features a clear indent on the flat surface of the bone.

In a previous study employing comparable µCT methods, evidence of a bone durophagous diet was inferred from two carnivoran coprolites of discrete sizes from the late Miocene, Spain (Abella et al. 2021). Evidence of bone durophagy is based on abundant skeletal inclusions including fragments that appeared to belong to larger bones while others display depressions resembling partial tooth marks. Similar to the Class I PSMP coprolites, the larger of the Spanish coprolites (BAT-3'9.178) preserves irregular bone fragments not identifiable to a specific anatomical bone but does show evidence of digestive corrosion (Abella et al. 2021). The smaller coprolite (BAT-3'10.153), which is comparable in length to the PSMP Class I coprolites exhibits more complete skeletal elements and has a greater proportion of bone inclusions relative to the larger coprolite at the same locality (Abella et al. 2021, fig. 4 and 6). Several medium-sized carnivores were suggested as the producer of the smaller coprolite though the most probable was *Prtictitherium crassum*, a member of the Hyaenidae.

These findings also seem to align with those of Lofgren et al. (2017), to the extent that some of the predators consumed the bones and that there was some sort of bone breaking occurring, especially in the smaller coprolites.

2.4.2 *Identity of the producer: additional insights*

Several different mammalian predators have been recovered from the PSMP site, belonging to eight different genera (Lofgren et al. 2017) including *Hyaenodon microdon* (Mellet, 1977), *Hyaenodon crucians* (Leidy, 1853), *Hesperocyon gregarius* (Cope, 1873), *Mustelavus priscus* (Clark, 1936, in Scott and Jepsen, 1936), *Brachyrhynchocyon dodgei* (Scott, 1898), *Paractis montanus* (Clark and Guensburg, 1972), *Daphoenictis tedfordi* (Hunt, 1974), and *Palaeogale sectoria* (Gervais, 1848, 1852). After estimating the overall body mass of the smaller predators and their prey mean mass (see Table 3), Lofgren et al. (2017) deduced that the smaller coprolites could have been produced by *Palaeogale sectoria, Paractis montanus, Hyaenodon crucians, Hyaenodon microdon,* and *Hesperocyon gregarius* (Lofgren et al. 2017). However, due to the abundance of dentigerous elements of *Hesperocyon gregarius,* representing over half the carnivorous specimens recovered, it was inferred as the main producer of the smaller coprolites (Lofgren et al. 2017).

Table 3. Summary of the main carnivorous species found in the PSMP. Data derived from LaGarry, 2004; Lofgren et al. 2017; Christison et al. 2022 (latter noted in bold).

Taxon	**Family**	**Body Mass (kg)**	**Mean prey focus mass (kg)**
Hyaenodon microdon	*Hyaenodontidae*	1.6 (**27.2**)	49.1
Hyaenodon crucians	*Hyaenodontidae*	3.3	NA
Hesperocyon gregarius	*Canidae*	3.0 (**3.5**)	6.4
Mustelavus priscus	*Mustelidae*	1.9	NA
Brachyrhynchocyon dodgei	*Amphicyonidae*	**13.9**	25.1
Daphoenictis tedfordi	*Amphicyonidae*	NA	NA
Paractis montanus	*Ursidae*	2.5	NA
Palaeogale sectoria	*Palaeogalidae*	1.7	NA

While the coprolite interior structures and bone inclusions observed herein did not elucidate any unambiguous details as to which taxon might have excreted the coprolites, it did reveal that at least the Class I producers had aggressive gastrointestinal environments that could digest bone material and cartilage. This is presumably comparable to the bone-crushing habits of modern spotted hyaenas (*Crocuta crocuta*), which are also known to consume (and occasionally regurgitate) indigestible materials such as hair (Kruuk, 1972; Silvestre et al. 2000). However, As noted by Wang et al. (2018) in their assessment of the California carnivoran coprolites, there is a paucity of literature investigating gastric pH across broader carnivore clades, and hence it is highly speculative to make further inferences as to the identity of the producer based on broad assumptions of a bone-dissolving gastrointestinal system alone.

2.4.3 *Taphonomic features and internal structures of the PSMP coprolites*

Pores are abundant within the internal structure of the coprolite samples and are known to frequently occur within the matrix of such fossils (Herbig, 1993). With few exceptions (inc. RAM 31211 and RAM 31212), pores made up the largest percentage of structural elements in the PSMP after the matrix (Figs 2.14A-B). As seen in Figure 2.7, the pores vary in size from as low as 0.19 mm to 19.6 mm and are distributed throughout the matrix, excluding where the space is occupied by skeletal remains. Notably, the exact origin of the pores remains speculative as they may have formed in different ways. The first mechanism is by the decay of some degradable materials within the scat, including smaller bone fragments, soft tissue (muscle, tendons, ligaments, etc.), or insect parts that might not have been digested, subsequently decayed, and formed these pores. Given the

abundance of decayed bone material in response to a presumably hyperacidic environment this seems unlikely. An alternative explanation is that the pores were already present at the time of excretion (including on the surface) caused by trapped gases within the scat, a product of bacterial respiration in the intestine (Herbig, 1993, Magondu, 2021). Gases formed in response to digestion are in no way unusual, however, the preservation of these pores and their relative abundance within a coprolite are often overlooked. While previous studies (Wang et al. 2018, Abella et al. 2021) have also used x-ray tomographic microscopy to examine internal features, their findings mostly discussed bone inclusions in the studied coprolite samples, with virtually no mention of other internal features such as pores. It is difficult to assess whether features such as pores were present within the coprolites of these previous studies, as they were not visible or extracted in rendered volumes (e.g. see Wang et al. 2018, figs 2D and 3C; Abella et al. 2021, fig 4A and D). However, it is also possible that the preservation of pores and their representation in µCT datasets is also dictated by the diagenesis of the specimens. As excess gas usually pertains to bacterial overgrowth within the gut, which may have deleterious consequences for the individual or indicate an intestinal disease, such pores may be useful in understanding the gut biome and physiological attributes of coprolite producers. A third explanation for the pores could be related to desiccation during the drying process. It has been noted that some surface pores can be created during the drying of a coprolite sample (Pratt, 1998). As the sample loses moisture smaller pores (possibly those formed by gases) are enlarged in conjunction with the reduction in overall coprolite volume.

Hair remains within the coprolite matrix are also preserved as pores. While only RAM 17540 received a targeted higher resolution scan, other coprolites from this collection exhibit similar structures. These small tube-like pores generally fall within the shaft shape and size range of hair, with distinct circular cross-sections. Because these pores are small, isolated, with many terminating without contacting the surface of the coprolite, it is possible to distinguish these structures from desiccation cracks or insect burrows. Hair molds can also be readily observed on the surface of select PSMP coprolites (see RAM 17540, Fig. 2.3C). Not all small pores within the coprolite are present in a tubelike structure so hairs cannot account for all the pores presents.

Like bones and teeth that are comparatively resistant to decay, keratinous material would have survived the digestive and early lithification process (Taru and Backwell, 2013). Though the hair eventually decayed, it was preserved long enough to form imprints of the shafts within the interior of the coprolite. This conforms with previous studies where hair structures have been found as casts and impressions both on the surface and interior of coprolites, often preserving exceptional details of the cuticular surface (Crooper et al. 1997; Taru and Backwell, 2013; Bajdek et al. 2016). Most of the pores display a silicon crust coating that implies secondary silicification during diagenesis. This indicates that the pores were there before the secondary silicification occurred. In the hair structure pores, it was likely that the pore was created before the crust developed around the pore as the hair would have decomposed before silicification could occur.

The preservation of bone inclusions within the coprolites varied across the two classes with no apparent pattern in the volume, type, or number of bone inclusions. The

coprolite size did not affect the number of bones preserved within the sample, though the Class II coprolites had more bone inclusions proportionally to their total volume compared to the larger Class I coprolites. Producers of the feces might have been responsible for the difference in preservation (Hunt et al. 2012). This can be seen in the different size of bones preserved in the different coprolite classes (Fig. 2.15A–D). It can also be seen with how well certain bones are preserved between the two classes. This was the case with these coprolites, but it is still not completely clear who produced the coprolites (Lofgren et al. 2017). Lofgren identified several potential producers in their initial study with teeth and jaw samples that were recovered from the same site.

2.4.4 *Evaluation of µCT and the analysis of coprolites*

The primary advantage that µCT affords in the present (and future) studies is the ability to reveal inclusions and internal structures such as pores and moldic remains of fossil hair that would not otherwise be attainable via disaggregation methods. These structures were readily visible in tomographic projections, in both standard and targeted higher resolution scans, and could be extracted to display their morphology as well as their distribution in three-dimensional space (Fig. 2.9). As hair structures represent external molds, destructive methods of extracting inclusions (whether by mechanical or chemical means) would impede the detection of such features at all. Even thin sectioning only provides a very shallow three-dimensional view of the internal composition of the coprolite matrix. As such, these features might be interpreted as ambiguous pores spaces that could not solely be attributed to the preserved remains of hair. Similarly, pores tend to be overlooked as contributing to the internal structure of coprolites because they too are lost via consumptive sampling methods. Pores are likely important taphonomic

features and hence understanding something about their abundance and distribution is also relevant to revealing the diagenetic history of the overall coprolite sample.

An additional benefit unique to µCT and subsequent segmentation of the data is the capacity to gather volumetric and geometric measurements (e.g., length, width, feret distances) via labeled voxels permitting more comprehensive quantitative analysis. Herein, extracting volumetric and feret diameters of the coprolites and their internal constituents facilitated comparisons between coprolite size classes. Moreover, the relative proportions of each inclusion were able to be calculated and compared to one another. This provides a more complete picture of the PSMP coprolite's internal composition than previously documented, for instance revealing pore space as the second largest inclusion after the matrix. While thin sectioning (Huisman et al. 2014), and observing internal pores along fractured or broken surfaces, does provide some insight into their general presence and cross-sectional size and shape, these data are limited with respect to assessing the quantity and distribution of the pores throughout a sample. The data provided by µCT and 3D segmentation comparisons allow for statistical tests that can be repeated across different coprolite specimens and compare preservation within sample groups.

Besides the quantitative advantage of producing volumetric renders of coprolites is the ability to survey and target regions of interest that might be well-suited to thin sectioning or elemental analyses (Shillito et al. 2020). Within our own sub-set of samples, certain coprolites possess minimal inclusions and consequently would offer a limited view of the internal heterogeneity observed in other samples. µCT scans provide a reference dataset to determine which coprolites would maximize data return whilst

minimizing consumptive sampling for thin sectioning and SEM analysis. This was imperative for the current study, as we were limited by the amount of destructive sample preparation that could be performed on the samples. Targeted sampling of specimen RAM 17540 enabled sectioning along a predetermined path that intersected a range of inclusions and taphonomic features comparable to other specimens within the sampled dataset.

Challenges with the methodology do persist, often owing to the attributes of the sample. For instance, due to the similarity in composition between the phosphatic matrix and bone inclusions, these features can be difficult to decern via standard segmentation techniques such as thresholding, as both materials occupy the same greyscale range. This is exacerbated by taphonomic processes caused during digestion wherein the bone margins become diffuse. Consequently, generic-level taxonomic information of skeletal inclusions is frequently not possible. Nevertheless, for coprolites and inclusions that have not been significantly diagenetically altered, µCT proves to be a powerful tool in extracting additional structural and taphonomic information that might be lost via physical extraction methods.

The results of this study support previous findings employing similar techniques comparing the results of mechanical extraction and µCT analysis. For example, studies of neolithic midden deposits from Swifterbant, Netherlands paired µCT and mechanical extraction methods to examine bone data from coprolites therein (Huisman et al. 2014). The results compiled from the µCT segmentation were very similar compared to the physical extraction of bones. Furthermore, identification of the skeletal components was not dependent on how the bones were extracted, but rather on how completely the bones

were preserved (Huisman et al. 2014). Bones with few distinguishable features as a consequence of the mastication and digestive processes are going to appear almost identical whether observed as virtually or physically extracted material. Similar results were documented by Abella et al. (2021), which albeit solely used µCT, but found many of the bones were not identifiable to a certain anatomical bone or taxon, and instead the authors relied on describing the general shape and features. The ability to only make broad identifications of bones present within the PSMP samples using µCT aligns with previous findings (Huisman et al. 2014; Abella et al. 2021), but further emphasizes that the limitation is associated with the degree of preservation and not the imaging technique. Finally, µCT may be instrumental in the long-term preservation and curation of coprolite samples. As demonstrated herein, it is desirable that prior to destructive sampling, a virtual record of the coprolite is retained for reference. Ultimately, this facilitates opportunities to share qualitative and quantitative µCT datasets via digital repositories. It is anticipated that this will enable greater standardization of methods and allows for more comparative analyses to expand the field of coprolite research.

2.5 Conclusion

X-ray tomographic microscopy of the twelve coprolites examined in this study provides further insights into the diet, feeding behavior, and physiology of the carnivoran producers from the Miocene Pipestone Spring Main Pocket, Montana. The application of µCT was a viable alternative to consumptive sampling and was able to differentiate internal structures, including bones and pores, from the overall matrix. Across the two coprolite size classes, several different bone types of varying quality are preserved. Although µCT methods were able to extract the skeletal inclusions in detail, the condition

of the bones as a result of the overall digestive process precluded taxonomic identification and hence limited descriptions to anatomical bone morphologies. A major benefit of the μCT methodology employed is the ability to extract details of internal structures that would be unattainable via consumptive sampling methods. Foremost is the presence of pores and hair-like structures within the coprolite matrix, which have been overlooked in previous μCT studies of coprolite specimens from other deposits.

The size, shape, and abundance of bone inclusions in conjunction with hair impressions suggest these predators consumed vertebrate prey. Depending on the size of the prey, the respective producers of the coprolite size classes appear to have adapted different feeding habits to maximize the return on nutrients. The larger coprolites contained comparatively fewer complete bones and were dominated by a fine-grained homogenous bone powder matrix suggesting high consumption of bone material via bone-crushing habits. Alternatively, the variability in the smaller coprolites containing both complete bone morphologies in greater proportions as well as fragmented bone implies both whole consumption and bone-crushing tendencies.

In retrospect, certain aspects of this study could have been improved through additional statistical metrics applied to the analysis of other inclusions (e.g., pores and hair). Additionally, new avenues of CT segmentation including machine and deep learning algorithms might offer more effective means of extracting the separate components of the coprolites. For instance, the hair structures proved more difficult than other inclusions using greyscale thresholding; a more focused effort on their extraction might elucidate details on their proclivity towards preservation.

Overall, application of µCT methodologies will allow for further standardization of coprolite studies. With the growth of virtual paleontology, an opportunity has presented itself for the expansion of coprolite research and the integration of novel qualitative and quantitative analyses. Where coprolite samples were once damaged or destroyed via traditional methods, µCT allows for their long-term preservation and promotes a means of sharing three-dimensional datasets via online repositories. Not only is µCT a powerful tool in future coprolite studies, but it is also fundamental to further the principals of reproducibility, accessibility, and collaborative science in the field.

2.6 Supplementary File

Table 1. Scanning parameters used for X-ray tomographic microscopy.

Sample	kV	W	Objective	Filter	Pixel um	Exposure seconds	Projections	Rotation degrees
17370	100	9	0.4X	LE5	30.12	1	1601	360
17405	100	9	0.4X	LE5	27.357	1	1601	360
17517	100	9	0.4X	LE5	28.693	1.25	1601	360
17540 High-Res	100	9	0.4X	LE5	3.4618	5	1601	360
17540 Hi-Res	100	9	0.4X	LE5	10.553	3	1601	360
17546	140	10	0.4X	LE5	31.005	1	1601	360
17547	140	10	0.4X	LE5	32.921	1	1601	360
18171	100	9	0.4X	LE5	27.024	1	1601	360
31211	100	9	0.4X	LE5	13.819	1	1601	360
31214	100	9	0.4X	LE5	13.819	1	1601	360
31209	100	9	0.4X	LE5	13.492	1	1601	360
31212	100	9	0.4X	LE5	13.919	1	1601	360
17540	80	7	0.4X	LE2	28.722	4	1601	360
17557	80	7	0.4X	LE2	28.722	1.25	1601	360

Table 2. Raw Coprolite Volume Data

Class	**Coprolite**	**Total Volume: Coprolite µm³**	**Total Volume: Bone µm³**	**Total Volume: Pores µm³**
Class I	RAM 17370	8,108,209,034,640.05	46,615,946,887.95	323,246,467,593.62
Class I	RAM 17405	10,502,736,094,520.70	20,398,230,276.29	1,099,926,186,772.68
Class I	RAM 17517	14,630,286,980,638.60	291,566,894,683.74	1,627,476,684,124.26
Class I	RAM 17540	11,125,865,983,934.10	55,236,052,858.03	1,041,149,867,944.45
Class I	RAM 17546	7,768,477,950,926.28	7,897,630,844.89	2,079,125,259,706.41
Class I	RAM 17547	10,059,968,878,409.90	222,489,985,566.49	595,959,198,629.95
Class I	RAM 18171	17,662,166,960,050.80	342,677,837,826.28	2,720,263,268,849.53
Class II	RAM 17557	1,324,730,338,578.82	80,811,807,625.53	326,570,475,701.93
Class II	RAM 31209	702,358,574,280.09	9,338,457,543.91	52,801,692,437.50
Class II	RAM 31211	913,026,460,677.63	126,152,958,679.72	124,956,422,778.16
Class II	RAM 31212	1,271,627,602,697.55	136,025,628,625.56	158,548,035,411.38
Class II	RAM 31214	1,564,427,192,284.42	17,755,730,900.63	177,268,943,893.65

Table 3. Coprolite Volumes based on percentages calculated from raw data

Class	Coprolite	Bone % of total Coprolite Volume	Pore % of total Coprolite Volume	Coprolite Matrix %
Class I	RAM 17370	0.57	3.99	95.44
Class I	RAM 17405	0.19	10.47	89.33
Class I	RAM 17517	1.99	11.12	86.88
Class I	RAM 17540	0.50	9.36	90.15
Class I	RAM 17546	0.10	26.76	73.13
Class I	RAM 17547	2.21	5.92	91.86
Class I	RAM 18171	1.94	15.40	82.66
Class II	RAM 17557	6.10	24.65	69.25
Class II	RAM 31209	1.33	7.52	91.15
Class II	RAM 31211	13.82	13.69	72.50
Class II	RAM 31212	10.70	12.47	76.83
Class II	RAM 31214	1.13	11.33	87.53

Table 4. Volumes used for Statistical Analysis for Figure 2.15A.

Class	Sample Name	Length (mm)	Width (mm)	Mass (g)	Coprolite Volume (mm^3)	Bone Volume (mm^3)	Pore Volume (mm^3)
Class I	RAM 17370	39.97	21.56	15.97	8108.209	46.61595	323.2465
Class I	RAM 17405	44.81	22.15	22	10502.74	20.39823	1099.926
Class I	RAM 17517	50.69	24.11	33.22	14630.29	291.5669	1627.477
Class I	RAM 17540	45.94	23.19	27.75	11125.87	55.23605	1041.15
Class I	RAM 17546	42.5	20.55	17.65	7768.478	7.897631	2079.125
Class I	RAM 17547	28.89	28.9	19.19	10059.97	222.49	595.9592
Class II	RAM 17557	26.14	11.05	3.61	17662.17	342.6778	2720.263
Class I	RAM 18171	64.36	24.03	39.14	1324.73	80.81181	326.5705
Class II	RAM 31209	14.38	11.26	1.68	702.3586	9.338458	52.80169
Class II	RAM 31211	22.65	9.91	2.08	913.0265	126.153	124.9564
Class II	RAM 31212	26.3	10.63	2.57	1271.628	136.0256	158.548
Class II	RAM 31214	24.03	10.71	3.27	1564.427	17.75573	177.2689

Table 5. Volumes used for Statistical Analysis for Figure 2.15B–D.

Sample Number	Class	Total Coprolite Volume (mm^3)	Total Bone Volume (mm^3)	Bone Volume (mm^3)	Name	Min Feret Diameter (mm)	Mean Feret Diameter (mm)	Max Feret Diameter (mm)
RAM 17370	Class I	8108.21	46.62	0.0088	974	0.41	0.51	0.57
RAM 17370	Class I	8108.21	46.62	0.220461	975	0.46	1.28	1.92
RAM 17370	Class I	8108.21	46.62	1.331316	976	1.09	2.01	3.26
RAM 17370	Class I	8108.21	46.62	1.397607	977	0.88	1.82	2.74
RAM 17370	Class I	8108.21	46.62	2.399243	978	1.07	2.45	4.4
RAM 17370	Class I	8108.21	46.62	3.449272	979	1.43	2.13	3.74
RAM 17370	Class I	8108.21	46.62	12.62109	980	1.25	4.12	6.91
RAM 17370	Class I	8108.21	46.62	25.08339	981	1.69	5.85	9.3
RAM 17405	Class I	10502.74	20.4	0.0043	1070	0.24	0.33	0.42
RAM 17405	Class I	10502.74	20.4	0.004545	1071	0.28	0.39	0.54
RAM 17405	Class I	10502.74	20.4	0.030936	1072	0.22	0.49	0.84
RAM 17405	Class I	10502.74	20.4	0.238605	1073	0.42	1.12	1.85
RAM 17405	Class I	10502.74	20.4	2.353603	1074	3.03	4.07	4.95
RAM 17405	Class I	10502.74	20.4	4.440859	1075	1.64	3.35	4.77
RAM 17405	Class I	10502.74	20.4	13.23366	1076	2.41	8.56	11.86
RAM 17517	Class I	14630.29	291.57	0.006891	9100	0.2	0.37	0.61
RAM 17517	Class I	14630.29	291.57	0.007034	9101	0.26	0.45	0.69
RAM 17517	Class I	14630.29	291.57	0.007106	9102	0.2	0.35	0.61
RAM 17517	Class I	14630.29	291.57	0.00744	9103	0.37	0.56	0.62
RAM 17517	Class I	14630.29	291.57	0.009061	9104	0.37	0.6	0.87
RAM 17517	Class I	14630.29	291.57	0.009252	9105	0.15	0.44	0.9
RAM 17517	Class I	14630.29	291.57	0.009276	9106	0.3	0.65	0.85
RAM 17517	Class I	14630.29	291.57	0.00949	9107	0.32	0.54	0.66
RAM 17517	Class I	14630.29	291.57	0.009538	9108	0.33	0.48	0.63
RAM 17517	Class I	14630.29	291.57	0.009991	9109	0.25	0.49	0.84
RAM 17517	Class I	14630.29	291.57	0.010897	9110	0.21	0.63	0.86
RAM 17517	Class I	14630.29	291.57	0.012972	9111	0.23	0.52	0.66
RAM 17517	Class I	14630.29	291.57	0.024846	9112	0.47	0.69	0.97
RAM 17517	Class I	14630.29	291.57	0.029448	9113	0.72	1.08	1.43
RAM 17517	Class I	14630.29	291.57	0.032214	9114	0.48	0.65	0.98
RAM 17517	Class I	14630.29	291.57	0.032858	9115	0.18	0.52	1.04
RAM 17517	Class I	14630.29	291.57	0.032906	9116	0.49	1.02	1.16
RAM 17517	Class I	14630.29	291.57	0.047714	9117	0.34	0.87	1.62

RAM 17517	Class I	14630.29	291.57	0.334377	9118	0.63	1.18	2.24
RAM 17517	Class I	14630.29	291.57	1.250522	9119	1.3	1.96	3.49
RAM 17517	Class I	14630.29	291.57	1.52779	9120	1.01	1.93	2.84
RAM 17517	Class I	14630.29	291.57	1.644034	9121	1.29	2.17	3.55
RAM 17517	Class I	14630.29	291.57	2.052235	9122	1.37	2.44	3.28
RAM 17517	Class I	14630.29	291.57	2.950735	9123	1.53	2.65	3.57
RAM 17517	Class I	14630.29	291.57	2.982043	9124	1.6	2.42	3.39
RAM 17517	Class I	14630.29	291.57	6.890937	9125	3.57	5.89	8.85
RAM 17517	Class I	14630.29	291.57	8.938999	9126	1.85	3.54	4.26
RAM 17517	Class I	14630.29	291.57	10.73504	9127	2.66	4	4.51
RAM 17517	Class I	14630.29	291.57	15.9818	9128	2.58	5.49	8.43
RAM 17517	Class I	14630.29	291.57	25.471	9129	3.22	5.07	6.67
RAM 17517	Class I	14630.29	291.57	40.07548	9130	3.32	9.43	13.68
RAM 17517	Class I	14630.29	291.57	57.98864	9131	4.91	7.24	8.83
RAM 17517	Class I	14630.29	291.57	111.5197	9132	5.7	7.89	11.41
RAM 17540	Class I	11125.87	55.24	0.006516	1533	0.27	0.4	0.5
RAM 17540	Class I	11125.87	55.24	0.007535	1534	0.29	0.42	0.54
RAM 17540	Class I	11125.87	55.24	0.011136	1535	0.14	0.38	0.67
RAM 17540	Class I	11125.87	55.24	0.015378	1536	0.32	0.79	0.93
RAM 17540	Class I	11125.87	55.24	0.127191	1537	0.66	1.24	1.85
RAM 17540	Class I	11125.87	55.24	7.3799	1538	1.79	3.31	4.79
RAM 17540	Class I	11125.87	55.24	8.893185	1539	1.41	4.4	7.42
RAM 17540	Class I	11125.87	55.24	10.94201	1540	3.05	4.62	6.65
RAM 17540	Class I	11125.87	55.24	13.16776	1541	2.47	4.43	7.73
RAM 17540	Class I	11125.87	55.24	14.50644	1542	2.05	4.87	7.32
RAM 17546	Class I	7768.48	7.9	0.003	716	0.22	0.37	0.43
RAM 17546	Class I	7768.48	7.9	0.122143	717	0.55	0.88	1.21
RAM 17546	Class I	7768.48	7.9	0.148371	718	0.56	0.95	1.77
RAM 17546	Class I	7768.48	7.9	0.251409	719	0.84	1.05	1.58
RAM 17546	Class I	7768.48	7.9	0.313911	720	0.84	1.48	2.16
RAM 17546	Class I	7768.48	7.9	0.444488	721	0.74	1.91	3.53
RAM 17546	Class I	7768.48	7.9	1.035619	722	0.92	3.04	4.55
RAM 17546	Class I	7768.48	7.9	5.529233	723	2.15	3.99	4.99
RAM 17547	Class I	10059.57	222.49	0.008706	5077	0.29	0.48	0.78
RAM 17547	Class I	10059.57	222.49	0.00999	5078	0.18	0.41	0.54
RAM 17547	Class I	10059.57	222.49	0.010026	5079	0.2	0.35	0.79
RAM 17547	Class I	10059.57	222.49	0.010847	5080	0.23	0.46	0.74
RAM 17547	Class I	10059.57	222.49	0.011275	5081	0.35	0.58	1.03
RAM 17547	Class I	10059.57	222.49	0.01131	5082	0.14	0.68	0.83
RAM 17547	Class I	10059.57	222.49	0.012702	5083	0.48	0.68	0.91
RAM 17547	Class I	10059.57	222.49	0.01313	5084	0.32	0.57	0.84

RAM 17547	Class I	10059.57	222.49	0.013201	5085	0.3	0.43	0.54
RAM 17547	Class I	10059.57	222.49	0.013594	5086	0.33	0.46	0.53
RAM 17547	Class I	10059.57	222.49	0.014771	5087	0.35	0.55	0.68
RAM 17547	Class I	10059.57	222.49	0.015235	5088	0.38	0.6	0.67
RAM 17547	Class I	10059.57	222.49	0.016841	5089	0.3	0.49	0.64
RAM 17547	Class I	10059.57	222.49	0.019981	5090	0.35	0.65	0.74
RAM 17547	Class I	10059.57	222.49	0.021836	5091	0.5	0.67	0.79
RAM 17547	Class I	10059.57	222.49	0.024512	5092	0.4	0.6	0.85
RAM 17547	Class I	10059.57	222.49	0.044885	5093	0.35	0.51	0.69
RAM 17547	Class I	10059.57	222.49	0.052449	5094	0.3	0.71	0.85
RAM 17547	Class I	10059.57	222.49	0.059228	5095	0.57	0.74	1.03
RAM 17547	Class I	10059.57	222.49	0.063866	5096	0.36	0.83	1.02
RAM 17547	Class I	10059.57	222.49	0.078852	5097	0.55	1.03	1.19
RAM 17547	Class I	10059.57	222.49	0.080457	5098	0.36	0.74	0.93
RAM 17547	Class I	10059.57	222.49	0.084239	5099	0.33	1.1	2.29
RAM 17547	Class I	10059.57	222.49	0.086166	5100	0.44	0.76	1.17
RAM 17547	Class I	10059.57	222.49	0.319867	5101	0.45	1.17	1.83
RAM 17547	Class I	10059.57	222.49	0.434327	5102	1.23	1.68	2.13
RAM 17547	Class I	10059.57	222.49	0.486383	5103	0.95	1.78	2.29
RAM 17547	Class I	10059.57	222.49	1.734846	5104	1.06	2.74	4.38
RAM 17547	Class I	10059.57	222.49	2.69227	5105	1.1	3.15	4.26
RAM 17547	Class I	10059.57	222.49	3.339782	5106	0.91	4.28	5.43
RAM 17547	Class I	10059.57	222.49	4.115919	5107	2.54	6.17	7.53
RAM 17547	Class I	10059.57	222.49	5.101744	5108	1.24	2.95	3.99
RAM 17547	Class I	10059.57	222.49	11.57008	5109	0.97	3.85	8.45
RAM 17547	Class I	10059.57	222.49	190.0806	5110	6.83	11.49	16.56
RAM 18171	Class I	17662.17	342.68	0.013598	1061	0.3	0.56	1
RAM 18171	Class I	17662.17	342.68	0.013716	1062	0.26	0.38	0.71
RAM 18171	Class I	17662.17	342.68	0.013775	1063	0.32	0.6	0.8
RAM 18171	Class I	17662.17	342.68	0.014229	1064	0.19	0.63	1.05
RAM 18171	Class I	17662.17	342.68	0.014604	1065	0.35	0.88	1.08
RAM 18171	Class I	17662.17	342.68	0.015295	1066	0.22	0.85	1.04
RAM 18171	Class I	17662.17	342.68	0.015315	1067	0.48	0.62	0.75
RAM 18171	Class I	17662.17	342.68	0.015887	1068	0.19	0.84	1.08
RAM 18171	Class I	17662.17	342.68	0.016262	1069	0.29	0.55	0.94
RAM 18171	Class I	17662.17	342.68	0.017328	1070	0.47	0.58	0.69
RAM 18171	Class I	17662.17	342.68	0.018867	1071	0.46	0.82	0.95
RAM 18171	Class I	17662.17	342.68	0.01938	1072	0.24	0.74	0.94
RAM 18171	Class I	17662.17	342.68	0.019834	1073	0.47	0.63	0.82
RAM 18171	Class I	17662.17	342.68	0.02088	1074	0.45	0.59	0.79
RAM 18171	Class I	17662.17	342.68	0.021413	1075	0.28	0.65	0.9

RAM 18171	Class I	17662.17	342.68	0.022617	1076	0.39	0.89	1.16
RAM 18171	Class I	17662.17	342.68	0.023327	1077	0.4	0.72	1.07
RAM 18171	Class I	17662.17	342.68	0.025064	1078	0.32	0.64	0.75
RAM 18171	Class I	17662.17	342.68	0.027393	1079	0.32	0.74	1.41
RAM 18171	Class I	17662.17	342.68	0.029268	1080	0.43	0.53	0.64
RAM 18171	Class I	17662.17	342.68	0.029505	1081	0.44	0.73	0.96
RAM 18171	Class I	17662.17	342.68	0.031123	1082	0.37	0.47	0.57
RAM 18171	Class I	17662.17	342.68	0.032228	1083	0.58	0.9	1.06
RAM 18171	Class I	17662.17	342.68	0.032406	1084	0.51	0.79	0.96
RAM 18171	Class I	17662.17	342.68	0.033452	1085	0.41	0.76	1.37
RAM 18171	Class I	17662.17	342.68	0.036057	1086	0.31	1.12	1.36
RAM 18171	Class I	17662.17	342.68	0.040912	1087	0.65	0.89	1.18
RAM 18171	Class I	17662.17	342.68	0.041681	1088	0.72	0.81	0.96
RAM 18171	Class I	17662.17	342.68	0.04401	1089	0.25	0.95	1.53
RAM 18171	Class I	17662.17	342.68	0.049359	1090	0.59	1.08	1.26
RAM 18171	Class I	17662.17	342.68	0.050681	1091	0.74	1.22	1.72
RAM 18171	Class I	17662.17	342.68	0.056503	1092	0.43	0.72	0.93
RAM 18171	Class I	17662.17	342.68	0.066864	1093	0.37	0.84	1.28
RAM 18171	Class I	17662.17	342.68	0.084192	1094	0.48	0.83	1.03
RAM 18171	Class I	17662.17	342.68	0.098796	1095	0.33	0.84	1.06
RAM 18171	Class I	17662.17	342.68	0.100947	1096	0.68	0.94	1.43
RAM 18171	Class I	17662.17	342.68	0.115966	1097	0.32	1.97	3.59
RAM 18171	Class I	17662.17	342.68	0.124886	1098	0.36	0.85	2
RAM 18171	Class I	17662.17	342.68	0.150898	1099	0.34	1.01	1.57
RAM 18171	Class I	17662.17	342.68	0.185553	1100	0.34	0.98	2.19
RAM 18171	Class I	17662.17	342.68	0.317308	1101	0.47	1.01	2.49
RAM 18171	Class I	17662.17	342.68	0.338662	1102	0.46	1.35	1.65
RAM 18171	Class I	17662.17	342.68	0.345846	1103	0.48	2.1	3.06
RAM 18171	Class I	17662.17	342.68	0.409749	1104	0.64	1.2	1.73
RAM 18171	Class I	17662.17	342.68	0.487705	1105	1.02	1.66	2.65
RAM 18171	Class I	17662.17	342.68	0.511308	1106	0.63	1.95	2.6
RAM 18171	Class I	17662.17	342.68	0.780363	1107	0.83	2.08	4.96
RAM 18171	Class I	17662.17	342.68	0.81042	1108	1.5	2.37	2.68
RAM 18171	Class I	17662.17	342.68	1.07606	1109	0.8	1.95	2.99
RAM 18171	Class I	17662.17	342.68	1.076731	1110	0.76	2	2.95
RAM 18171	Class I	17662.17	342.68	1.428991	1111	1.42	2.58	2.86
RAM 18171	Class I	17662.17	342.68	1.77681	1112	1.05	2.82	3.5
RAM 18171	Class I	17662.17	342.68	1.854153	1113	1.31	2.07	2.37
RAM 18171	Class I	17662.17	342.68	1.936155	1114	1.13	4.95	8.56
RAM 18171	Class I	17662.17	342.68	2.856837	1115	0.9	2.45	5.57
RAM 18171	Class I	17662.17	342.68	3.323405	1116	1.46	3.62	4.23

RAM 18171	Class I	17662.17	342.68	3.494216	1117	1.35	4.16	6.87
RAM 18171	Class I	17662.17	342.68	3.691808	1118	1.72	2.58	3.42
RAM 18171	Class I	17662.17	342.68	3.724648	1119	1.3	3.61	4.8
RAM 18171	Class I	17662.17	342.68	4.317918	1120	1	6.32	9.41
RAM 18171	Class I	17662.17	342.68	7.057289	1121	1.85	5.93	8.63
RAM 18171	Class I	17662.17	342.68	7.65348	1122	2.25	7.57	9.32
RAM 18171	Class I	17662.17	342.68	7.812982	1123	2.62	4.77	6.25
RAM 18171	Class I	17662.17	342.68	9.570471	1124	2.54	5.39	6.39
RAM 18171	Class I	17662.17	342.68	10.69703	1125	1.67	4.38	6.88
RAM 18171	Class I	17662.17	342.68	13.4934	1126	1.9	4.06	5.72
RAM 18171	Class I	17662.17	342.68	18.27538	1127	1.42	6.9	11.15
RAM 18171	Class I	17662.17	342.68	21.59983	1128	2.68	8.68	10.45
RAM 18171	Class I	17662.17	342.68	23.501	1129	3.01	9.3	12.35
RAM 18171	Class I	17662.17	342.68	51.7922	1130	3.02	11.29	13.72
RAM 18171	Class I	17662.17	342.68	63.92807	1131	3.49	11.81	15.63
RAM 18171	Class I	17662.17	342.68	69.16332	1132	6.76	10.06	16.19
RAM 17557	Class II	1324.73	80.81	0.010568	1638	0.42	0.52	0.57
RAM 17557	Class II	1324.73	80.81	0.017297	1639	0.46	0.58	0.78
RAM 17557	Class II	1324.73	80.81	0.028694	1640	0.39	0.51	0.69
RAM 17557	Class II	1324.73	80.81	0.031158	1641	0.03	0.97	1.86
RAM 17557	Class II	1324.73	80.81	0.065396	1642	0.46	0.67	1.1
RAM 17557	Class II	1324.73	80.81	0.066699	1643	0.26	0.72	1.1
RAM 17557	Class II	1324.73	80.81	0.087266	1644	0.35	0.86	1.15
RAM 17557	Class II	1324.73	80.81	0.089043	1645	0.35	0.88	1.17
RAM 17557	Class II	1324.73	80.81	0.097004	1646	0.38	0.67	1.02
RAM 17557	Class II	1324.73	80.81	0.101056	1647	0.44	0.97	1.16
RAM 17557	Class II	1324.73	80.81	0.127499	1648	0.46	0.9	1.24
RAM 17557	Class II	1324.73	80.81	0.139441	1649	0.14	1.06	2.07
RAM 17557	Class II	1324.73	80.81	0.190147	1650	0.51	1.17	1.71
RAM 17557	Class II	1324.73	80.81	0.292648	1651	0.64	0.97	1.17
RAM 17557	Class II	1324.73	80.81	0.352026	1652	0.69	1.43	1.67
RAM 17557	Class II	1324.73	80.81	0.507982	1653	0.71	1.29	1.88
RAM 17557	Class II	1324.73	80.81	0.579207	1654	0.54	1.59	2.33
RAM 17557	Class II	1324.73	80.81	0.737983	1655	0.88	1.74	2.63
RAM 17557	Class II	1324.73	80.81	0.941849	1656	0.89	1.99	2.55
RAM 17557	Class II	1324.73	80.81	1.100909	1657	0.85	2.37	3
RAM 17557	Class II	1324.73	80.81	2.131564	1658	1.22	2.7	3.69
RAM 17557	Class II	1324.73	80.81	2.834716	1659	1.04	3.8	4.93
RAM 17557	Class II	1324.73	80.81	4.390792	1660	1.87	3.46	5.51
RAM 17557	Class II	1324.73	80.81	4.465714	1661	2.28	3.44	4.65
RAM 17557	Class II	1324.73	80.81	4.977416	1662	1.8	3.56	4.16

RAM 17557	Class II	1324.73	80.81	8.232564	1663	2	5.43	7.14
RAM 17557	Class II	1324.73	80.81	9.043075	1664	1.92	4.31	5.24
RAM 17557	Class II	1324.73	80.81	11.62023	1665	3.37	4.63	6.64
RAM 17557	Class II	1324.73	80.81	17.49237	1666	3.99	8.13	11.33
RAM 31209	Class II	702.36	9.34	0.00291	3469	0.16	0.2	0.26
RAM 31209	Class II	702.36	9.34	0.004043	3470	0.18	0.29	0.36
RAM 31209	Class II	702.36	9.34	0.007046	3471	0.15	0.35	0.73
RAM 31209	Class II	702.36	9.34	0.007346	3472	0.19	0.29	0.43
RAM 31209	Class II	702.36	9.34	0.009989	3473	0.31	0.46	0.65
RAM 31209	Class II	702.36	9.34	0.010413	3474	0.13	0.33	0.6
RAM 31209	Class II	702.36	9.34	0.017312	3475	0.27	0.43	0.75
RAM 31209	Class II	702.36	9.34	0.027168	3476	0.3	0.44	0.6
RAM 31209	Class II	702.36	9.34	0.034313	3477	0.38	0.56	0.77
RAM 31209	Class II	702.36	9.34	0.043768	3478	0.29	0.67	1.1
RAM 31209	Class II	702.36	9.34	0.047487	3479	0.47	0.7	1.05
RAM 31209	Class II	702.36	9.34	0.049695	3480	0.27	0.77	1.46
RAM 31209	Class II	702.36	9.34	0.050181	3481	0.39	0.56	0.82
RAM 31209	Class II	702.36	9.34	0.06417	3482	0.45	0.7	1.23
RAM 31209	Class II	702.36	9.34	0.068947	3483	0.43	0.63	0.95
RAM 31209	Class II	702.36	9.34	0.07032	3484	0.51	0.69	0.97
RAM 31209	Class II	702.36	9.34	0.086886	3485	0.5	0.74	0.88
RAM 31209	Class II	702.36	9.34	0.088792	3486	0.45	0.65	0.87
RAM 31209	Class II	702.36	9.34	0.091685	3487	0.41	0.78	1.16
RAM 31209	Class II	702.36	9.34	0.108634	3488	0.53	0.67	0.79
RAM 31209	Class II	702.36	9.34	0.137325	3489	0.47	1.06	1.49
RAM 31209	Class II	702.36	9.34	0.176484	3490	0.69	0.9	1.21
RAM 31209	Class II	702.36	9.34	0.208058	3491	0.51	1.14	1.32
RAM 31209	Class II	702.36	9.34	0.266896	3492	0.67	1.06	1.96
RAM 31209	Class II	702.36	9.34	0.290435	3493	0.9	1.16	1.83
RAM 31209	Class II	702.36	9.34	0.30757	3494	0.77	1.08	1.54
RAM 31209	Class II	702.36	9.34	0.35657	3495	0.88	1.18	1.55
RAM 31209	Class II	702.36	9.34	0.381334	3496	0.74	1.05	1.7
RAM 31209	Class II	702.36	9.34	0.384927	3497	0.93	1.42	2.1
RAM 31209	Class II	702.36	9.34	0.412334	3498	0.63	1.37	1.76
RAM 31209	Class II	702.36	9.34	0.47197	3499	0.82	1.95	2.75
RAM 31209	Class II	702.36	9.34	0.803037	3500	1.06	1.58	2.48
RAM 31209	Class II	702.36	9.34	4.163837	3501	1.29	3.87	5.99
RAM 31211	Class II	913.03	126.15	0.006302	17716	0.18	0.27	0.42
RAM 31211	Class II	913.03	126.15	0.006737	17717	0.39	0.76	0.98
RAM 31211	Class II	913.03	126.15	0.007331	17718	0.2	0.32	0.36
RAM 31211	Class II	913.03	126.15	0.007357	17719	0.42	0.57	0.79

RAM 31211	Class II	913.03	126.15	0.007621	17720	0.25	0.39	0.43
RAM 31211	Class II	913.03	126.15	0.007737	17721	0.28	0.43	0.69
RAM 31211	Class II	913.03	126.15	0.008313	17722	0.44	0.64	0.74
RAM 31211	Class II	913.03	126.15	0.008656	17723	0.22	0.31	0.41
RAM 31211	Class II	913.03	126.15	0.008753	17724	0.44	0.77	0.98
RAM 31211	Class II	913.03	126.15	0.01069	17725	0.3	0.47	0.63
RAM 31211	Class II	913.03	126.15	0.01126	17726	0.23	0.34	0.53
RAM 31211	Class II	913.03	126.15	0.011917	17727	0.2	0.36	0.64
RAM 31211	Class II	913.03	126.15	0.012007	17728	0.32	0.66	0.89
RAM 31211	Class II	913.03	126.15	0.013218	17729	0.17	0.34	0.58
RAM 31211	Class II	913.03	126.15	0.013313	17730	0.3	0.37	0.46
RAM 31211	Class II	913.03	126.15	0.013422	17731	0.31	0.42	0.63
RAM 31211	Class II	913.03	126.15	0.01467	17732	0.24	0.38	0.47
RAM 31211	Class II	913.03	126.15	0.016422	17733	0.32	0.48	0.66
RAM 31211	Class II	913.03	126.15	0.018562	17734	0.23	0.52	1.08
RAM 31211	Class II	913.03	126.15	0.019085	17735	0.25	0.46	0.76
RAM 31211	Class II	913.03	126.15	0.020515	17736	0.22	0.48	0.81
RAM 31211	Class II	913.03	126.15	0.020753	17737	0.27	0.4	0.69
RAM 31211	Class II	913.03	126.15	0.026574	17738	0.21	0.64	0.82
RAM 31211	Class II	913.03	126.15	0.038431	17739	0.28	0.5	0.84
RAM 31211	Class II	913.03	126.15	0.04012	17740	0.39	0.55	0.93
RAM 31211	Class II	913.03	126.15	0.047833	17741	0.36	0.65	1.08
RAM 31211	Class II	913.03	126.15	0.049483	17742	0.36	0.79	1.01
RAM 31211	Class II	913.03	126.15	0.05014	17743	0.41	0.49	0.61
RAM 31211	Class II	913.03	126.15	0.052467	17744	0.39	0.6	0.98
RAM 31211	Class II	913.03	126.15	0.057582	17745	0.42	0.57	0.7
RAM 31211	Class II	913.03	126.15	0.058131	17746	0.41	0.62	0.84
RAM 31211	Class II	913.03	126.15	0.063021	17747	0.28	0.94	1.27
RAM 31211	Class II	913.03	126.15	0.068035	17748	0.39	0.61	1.04
RAM 31211	Class II	913.03	126.15	0.069531	17749	0.54	1.21	1.6
RAM 31211	Class II	913.03	126.15	0.083966	17750	0.39	0.8	1.52
RAM 31211	Class II	913.03	126.15	0.084414	17751	0.39	0.65	1.05
RAM 31211	Class II	913.03	126.15	0.087331	17752	0.49	0.92	1.42
RAM 31211	Class II	913.03	126.15	0.088581	17753	0.53	0.81	1.34
RAM 31211	Class II	913.03	126.15	0.08945	17754	0.41	0.56	0.74
RAM 31211	Class II	913.03	126.15	0.115522	17755	0.49	1.14	1.55
RAM 31211	Class II	913.03	126.15	0.128443	17756	0.75	1.31	1.92
RAM 31211	Class II	913.03	126.15	0.132781	17757	0.61	0.76	1.14
RAM 31211	Class II	913.03	126.15	0.146348	17758	0.41	1.02	1.29
RAM 31211	Class II	913.03	126.15	0.153491	17759	0.61	0.89	1.2
RAM 31211	Class II	913.03	126.15	0.15465	17760	0.63	0.87	1.29

RAM 31211	Class II	913.03	126.15	0.157867	17761	0.39	0.96	1.37
RAM 31211	Class II	913.03	126.15	0.159078	17762	0.47	1.24	2.15
RAM 31211	Class II	913.03	126.15	0.177667	17763	0.78	1.06	1.43
RAM 31211	Class II	913.03	126.15	0.182045	17764	0.72	1.11	1.6
RAM 31211	Class II	913.03	126.15	0.204125	17765	0.4	0.79	1.37
RAM 31211	Class II	913.03	126.15	0.212575	17766	0.74	0.95	1.23
RAM 31211	Class II	913.03	126.15	0.220848	17767	0.58	1.34	2.15
RAM 31211	Class II	913.03	126.15	0.245881	17768	0.48	1.23	1.64
RAM 31211	Class II	913.03	126.15	0.271645	17769	0.52	1.15	2.25
RAM 31211	Class II	913.03	126.15	0.293844	17770	0.56	1.55	1.83
RAM 31211	Class II	913.03	126.15	0.310925	17771	0.74	1.04	1.42
RAM 31211	Class II	913.03	126.15	0.321286	17772	0.63	1.36	1.66
RAM 31211	Class II	913.03	126.15	0.376522	17773	0.75	1.38	2.03
RAM 31211	Class II	913.03	126.15	0.451885	17774	1.14	1.99	2.56
RAM 31211	Class II	913.03	126.15	0.672703	17775	0.66	2.16	4.83
RAM 31211	Class II	913.03	126.15	0.695023	17776	0.89	1.72	2.44
RAM 31211	Class II	913.03	126.15	0.69696	17777	0.82	1.57	1.95
RAM 31211	Class II	913.03	126.15	0.713562	17778	1.11	2.3	2.82
RAM 31211	Class II	913.03	126.15	1.079567	17779	0.77	1.86	2.34
RAM 31211	Class II	913.03	126.15	1.434859	17780	0.98	2.67	4.7
RAM 31211	Class II	913.03	126.15	1.831473	17781	0.88	2.37	2.93
RAM 31211	Class II	913.03	126.15	1.859776	17782	0.97	2.53	3.92
RAM 31211	Class II	913.03	126.15	2.49261	17783	1.49	2.86	4.33
RAM 31211	Class II	913.03	126.15	4.891443	17784	2.36	3.02	4.05
RAM 31211	Class II	913.03	126.15	7.218844	17785	2.52	5.44	6.45
RAM 31211	Class II	913.03	126.15	18.79554	17786	4.26	5.31	7.73
RAM 31211	Class II	913.03	126.15	77.5388	17787	6.08	11.85	14.2
RAM 31212	Class II	1217.63	136.03	0.004954	1770	0.23	0.36	0.56
RAM 31212	Class II	1217.63	136.03	0.005256	1771	0.34	0.46	0.6
RAM 31212	Class II	1217.63	136.03	0.005347	1772	0.2	0.36	0.51
RAM 31212	Class II	1217.63	136.03	0.005587	1773	0.18	0.3	0.35
RAM 31212	Class II	1217.63	136.03	0.0058	1774	0.19	0.43	0.69
RAM 31212	Class II	1217.63	136.03	0.006566	1775	0.18	0.28	0.47
RAM 31212	Class II	1217.63	136.03	0.007443	1776	0.2	0.27	0.39
RAM 31212	Class II	1217.63	136.03	0.007901	1777	0.18	0.57	0.71
RAM 31212	Class II	1217.63	136.03	0.008209	1778	0.21	0.3	0.48
RAM 31212	Class II	1217.63	136.03	0.008357	1779	0.18	0.58	0.75
RAM 31212	Class II	1217.63	136.03	0.009271	1780	0.16	0.27	0.49
RAM 31212	Class II	1217.63	136.03	0.01032	1781	0.21	0.44	0.68
RAM 31212	Class II	1217.63	136.03	0.011682	1782	0.24	0.38	0.47
RAM 31212	Class II	1217.63	136.03	0.011714	1783	0.2	0.41	0.74

RAM 31212	Class II	1217.63	136.03	0.012043	1784	0.31	0.5	0.88
RAM 31212	Class II	1217.63	136.03	0.012348	1785	0.19	0.44	0.82
RAM 31212	Class II	1217.63	136.03	0.012547	1786	0.22	0.4	0.64
RAM 31212	Class II	1217.63	136.03	0.012685	1787	0.22	0.38	0.77
RAM 31212	Class II	1217.63	136.03	0.013014	1788	0.39	0.73	0.83
RAM 31212	Class II	1217.63	136.03	0.01316	1789	0.18	0.58	0.8
RAM 31212	Class II	1217.63	136.03	0.018893	1790	0.27	0.51	0.94
RAM 31212	Class II	1217.63	136.03	0.022593	1791	0.24	0.38	0.56
RAM 31212	Class II	1217.63	136.03	0.022833	1792	0.27	0.64	0.96
RAM 31212	Class II	1217.63	136.03	0.023267	1793	0.37	0.5	0.75
RAM 31212	Class II	1217.63	136.03	0.02571	1794	0.22	0.5	1.08
RAM 31212	Class II	1217.63	136.03	0.026273	1795	0.28	0.62	0.77
RAM 31212	Class II	1217.63	136.03	0.028795	1796	0.29	0.65	0.86
RAM 31212	Class II	1217.63	136.03	0.029024	1797	0.22	0.5	1
RAM 31212	Class II	1217.63	136.03	0.029159	1798	0.31	0.51	0.89
RAM 31212	Class II	1217.63	136.03	0.029547	1799	0.33	0.53	0.8
RAM 31212	Class II	1217.63	136.03	0.038319	1800	0.39	0.52	0.65
RAM 31212	Class II	1217.63	136.03	0.038589	1801	0.33	0.53	0.78
RAM 31212	Class II	1217.63	136.03	0.040398	1802	0.26	0.51	0.85
RAM 31212	Class II	1217.63	136.03	0.04566	1803	0.43	0.55	0.74
RAM 31212	Class II	1217.63	136.03	0.046633	1804	0.4	0.6	1.01
RAM 31212	Class II	1217.63	136.03	0.06154	1805	0.23	0.8	1.09
RAM 31212	Class II	1217.63	136.03	0.062204	1806	0.36	0.64	0.84
RAM 31212	Class II	1217.63	136.03	0.06493	1807	0.33	0.78	1.09
RAM 31212	Class II	1217.63	136.03	0.065755	1808	0.46	0.66	0.88
RAM 31212	Class II	1217.63	136.03	0.071221	1809	0.74	0.97	1.48
RAM 31212	Class II	1217.63	136.03	0.084141	1810	0.63	0.83	1.14
RAM 31212	Class II	1217.63	136.03	0.090532	1811	0.69	0.98	1.22
RAM 31212	Class II	1217.63	136.03	0.092937	1812	0.31	0.76	1.19
RAM 31212	Class II	1217.63	136.03	0.105137	1813	0.29	0.74	2.06
RAM 31212	Class II	1217.63	136.03	0.114815	1814	0.28	1.18	2.58
RAM 31212	Class II	1217.63	136.03	0.133209	1815	0.58	1.11	1.77
RAM 31212	Class II	1217.63	136.03	0.15609	1816	0.54	0.83	1.01
RAM 31212	Class II	1217.63	136.03	0.157967	1817	0.45	0.97	1.4
RAM 31212	Class II	1217.63	136.03	0.159286	1818	0.47	0.82	1.52
RAM 31212	Class II	1217.63	136.03	0.235593	1819	0.43	1.26	1.68
RAM 31212	Class II	1217.63	136.03	0.28739	1820	0.46	0.98	2.09
RAM 31212	Class II	1217.63	136.03	0.338192	1821	0.62	1.28	2.11
RAM 31212	Class II	1217.63	136.03	0.386117	1822	0.61	1.91	2.53
RAM 31212	Class II	1217.63	136.03	0.404829	1823	0.61	1.44	2.05
RAM 31212	Class II	1217.63	136.03	0.515448	1824	0.67	1.77	2

RAM 31212	Class II	1217.63	136.03	0.60485	1825	1.26	1.74	1.97
RAM 31212	Class II	1217.63	136.03	0.656264	1826	0.61	1.89	3.36
RAM 31212	Class II	1217.63	136.03	0.731633	1827	0.83	1.36	1.76
RAM 31212	Class II	1217.63	136.03	0.953359	1828	1.38	1.81	2.02
RAM 31212	Class II	1217.63	136.03	1.444901	1829	1.07	2.25	3.03
RAM 31212	Class II	1217.63	136.03	1.935421	1830	1.24	2.16	3.75
RAM 31212	Class II	1217.63	136.03	1.946181	1831	1.37	2.49	3.16
RAM 31212	Class II	1217.63	136.03	2.606201	1832	1.63	3.03	4.44
RAM 31212	Class II	1217.63	136.03	4.850289	1833	1.87	4.49	6.74
RAM 31212	Class II	1217.63	136.03	7.409774	1834	2.73	3.91	4.91
RAM 31212	Class II	1217.63	136.03	7.673217	1835	2.52	5.27	7.89
RAM 31212	Class II	1217.63	136.03	100.3426	1836	8.87	19.67	25.73
RAM 31214	Class II	1564.43	17.06	0.046672	17263	0.4	0.7	1.02
RAM 31214	Class II	1564.43	17.06	0.049134	17264	0.24	0.63	0.94
RAM 31214	Class II	1564.43	17.06	0.049567	17265	0.25	0.73	1.22
RAM 31214	Class II	1564.43	17.06	0.051137	17266	0.33	0.64	0.94
RAM 31214	Class II	1564.43	17.06	0.054821	17267	0.4	0.71	0.98
RAM 31214	Class II	1564.43	17.06	0.05637	17268	0.37	0.68	1.4
RAM 31214	Class II	1564.43	17.06	0.058352	17269	0.26	0.83	1.41
RAM 31214	Class II	1564.43	17.06	0.059606	17270	0.28	1.14	1.39
RAM 31214	Class II	1564.43	17.06	0.061453	17271	0.44	0.73	0.9
RAM 31214	Class II	1564.43	17.06	0.06244	17272	0.56	1	1.18
RAM 31214	Class II	1564.43	17.06	0.068232	17273	0.58	1.01	1.4
RAM 31214	Class II	1564.43	17.06	0.068531	17274	0.45	0.67	0.77
RAM 31214	Class II	1564.43	17.06	0.068657	17275	0.47	0.62	0.85
RAM 31214	Class II	1564.43	17.06	0.071869	17276	0.36	0.66	0.87
RAM 31214	Class II	1564.43	17.06	0.072318	17277	0.29	0.59	1.15
RAM 31214	Class II	1564.43	17.06	0.076923	17278	0.44	0.65	0.9
RAM 31214	Class II	1564.43	17.06	0.078303	17279	0.45	0.79	0.91
RAM 31214	Class II	1564.43	17.06	0.078685	17280	0.39	1.07	1.67
RAM 31214	Class II	1564.43	17.06	0.079823	17281	0.43	0.75	1.1
RAM 31214	Class II	1564.43	17.06	0.081108	17282	0.42	0.82	1.23
RAM 31214	Class II	1564.43	17.06	0.082736	17283	0.58	0.95	1.51
RAM 31214	Class II	1564.43	17.06	0.087652	17284	0.47	0.91	1.09
RAM 31214	Class II	1564.43	17.06	0.090503	17285	0.37	0.83	1.15
RAM 31214	Class II	1564.43	17.06	0.094435	17286	0.48	0.83	1.59
RAM 31214	Class II	1564.43	17.06	0.09743	17287	0.39	0.91	1.39
RAM 31214	Class II	1564.43	17.06	0.100681	17288	0.42	0.62	1.11
RAM 31214	Class II	1564.43	17.06	0.10494	17289	0.53	0.81	1.22
RAM 31214	Class II	1564.43	17.06	0.106355	17290	0.42	0.78	1.12
RAM 31214	Class II	1564.43	17.06	0.109492	17291	0.57	0.91	1.25

RAM 31214	Class II	1564.43	17.06	0.111561	17292	0.31	0.85	1.42
RAM 31214	Class II	1564.43	17.06	0.127585	17293	0.73	1.35	1.67
RAM 31214	Class II	1564.43	17.06	0.133267	17294	0.46	1.07	1.43
RAM 31214	Class II	1564.43	17.06	0.144611	17295	0.76	1.27	1.52
RAM 31214	Class II	1564.43	17.06	0.148565	17296	0.47	1.01	1.58
RAM 31214	Class II	1564.43	17.06	0.150776	17297	0.43	1.06	1.43
RAM 31214	Class II	1564.43	17.06	0.164295	17298	0.65	0.97	1.41
RAM 31214	Class II	1564.43	17.06	0.164913	17299	0.73	0.97	1.2
RAM 31214	Class II	1564.43	17.06	0.166137	17300	0.83	1.15	1.43
RAM 31214	Class II	1564.43	17.06	0.170655	17301	0.44	1.15	1.39
RAM 31214	Class II	1564.43	17.06	0.197905	17302	0.76	1.03	1.42
RAM 31214	Class II	1564.43	17.06	0.198097	17303	0.55	1.05	1.45
RAM 31214	Class II	1564.43	17.06	0.204753	17304	0.74	1.34	1.68
RAM 31214	Class II	1564.43	17.06	0.205497	17305	0.56	1.47	2.03
RAM 31214	Class II	1564.43	17.06	0.210342	17306	0.5	0.98	1.37
RAM 31214	Class II	1564.43	17.06	0.216454	17307	0.58	1.19	1.48
RAM 31214	Class II	1564.43	17.06	0.217911	17308	0.82	1.14	1.34
RAM 31214	Class II	1564.43	17.06	0.231348	17309	0.47	0.97	1.28
RAM 31214	Class II	1564.43	17.06	0.268647	17310	0.45	1.43	1.86
RAM 31214	Class II	1564.43	17.06	0.269148	17311	0.59	1	1.94
RAM 31214	Class II	1564.43	17.06	0.273716	17312	0.51	0.83	1.53
RAM 31214	Class II	1564.43	17.06	0.281156	17313	0.57	1.49	1.84
RAM 31214	Class II	1564.43	17.06	0.324139	17314	0.56	1.44	1.73
RAM 31214	Class II	1564.43	17.06	0.333657	17315	0.75	1.31	1.87
RAM 31214	Class II	1564.43	17.06	0.372344	17316	0.71	1.41	3.07
RAM 31214	Class II	1564.43	17.06	0.400784	17317	0.77	1.3	1.96
RAM 31214	Class II	1564.43	17.06	0.425619	17318	0.56	1.73	2.53
RAM 31214	Class II	1564.43	17.06	0.444131	17319	0.54	1.69	2.36
RAM 31214	Class II	1564.43	17.06	0.525239	17320	0.9	1.55	1.77
RAM 31214	Class II	1564.43	17.06	0.591321	17321	1	1.46	1.75
RAM 31214	Class II	1564.43	17.06	0.592105	17322	1.17	2.08	3.07
RAM 31214	Class II	1564.43	17.06	0.849175	17323	1.4	1.69	1.87
RAM 31214	Class II	1564.43	17.06	1.144583	17324	1.04	2.57	2.98
RAM 31214	Class II	1564.43	17.06	1.506443	17325	1.25	2.95	4.34
RAM 31214	Class II	1564.43	17.06	1.859106	17326	1.01	2.13	3.41

R-code Inputs. Below is a copy of the packages and r-code used in RStudio to conduct statistical analyses and create corresponding figures.

```
setwd("C://Users//huntleyj//OneDrive - University of Missouri//Active Research//Jeremy Webb")

#Packages
library(ggplot2)
library(ggthemes)

Coprolites <- read.csv("Coprolites.csv", header = TRUE, sep = ",")
attach(Coprolites)

Bones <- read.csv("Bones.csv", header = TRUE, sep = ",")
attach(Bones)

#Are there two different size classes of coprolites?
attach(Coprolites)

ggplot(data = Coprolites) + geom_point(aes(Length..mm., Width..mm., color=Class, size=Mass..g.)) + xlab("Length (mm)") + ylab("Width (mm)") +
  scale_x_log10() + scale_y_log10() + scale_color_colorblind() + theme_classic() +
guides(size=guide_legend(title="Mass (g)")) +
  theme(axis.title = element_text(size = 15)) + theme(axis.text = element_text(size = 15))


#Are there differences in the proportion of skeletal fragments between classes?
attach(Coprolites)
Coprolites$Skeletal.Proportion <-
(Coprolites$Bone.Volume..mm3./Coprolites$Coprolite.Volume..mm3.)

ggplot(data = Coprolites) + geom_point(aes(Class, Skeletal.Proportion, color=Class, size=Mass..g.), alpha=0.7) + xlab("") + ylab("Proportion of Skeletal Material") +
  ylim(c(0, 0.15)) + scale_color_colorblind() + theme_classic() +
guides(size=guide_legend(title="Mass (g)")) +
  theme(axis.title = element_text(size = 15)) + theme(axis.text = element_text(size = 15))

median(Coprolites$Skeletal.Proportion, Class=="Class I")
median(Coprolites$Skeletal.Proportion, Class=="Class II")
wilcox.test(Skeletal.Proportion ~ Class)
  #There is considerable overlap in the proportion of skeletal material between the two groups. The Wilcoxon test of median values did not return a significant difference. The sample sizes are small (5 and 7).

#Are there differences in bone size distribution between classes?
attach(Bones)
```

```
#By bone volume
ggplot(data = Bones) + geom_boxplot(aes(Class, `Bone.Volume..mm³.`, fill=Class)) +
scale_y_log10() + xlab("") + ylab("Bone Volume (mm3)") +
  scale_fill_colorblind() + theme_classic() + theme(axis.title = element_text(size = 15)) +
theme(axis.text = element_text(size = 15))

median(subset(Bones$`Bone.Volume..mm³.`, Class=="Class I"))
median(subset(Bones$`Bone.Volume..mm³.`, Class=="Class II"))
wilcox.test(Bones$`Bone.Volume..mm³.` ~ Class)
  #There is no significant (p=0.1757) difference in median bone volume comparing Class
I (0.09987167mm^3) and Class II (0.09443454mm^3)

#By max feret volume
ggplot(data = Bones) + geom_boxplot(aes(Class, Max.Feret.Diameter..mm., fill=Class))
+ scale_y_log10() + xlab("") + ylab("Maximum Feret Diameter (mm)") +
  scale_fill_colorblind() + theme_classic() + theme(axis.title = element_text(size = 15)) +
theme(axis.text = element_text(size = 15))


median(subset(Bones$Max.Feret.Diameter..mm., Class=="Class I"))
median(subset(Bones$Max.Feret.Diameter..mm., Class=="Class II"))
wilcox.test(Max.Feret.Diameter..mm. ~ Class)
  #The median Maximum Feret Diameter value for Class I (1.575 mm) is significantly
(p=0.001863) larger than that for Class II (1.25 mm)

#By mean feret diameter
ggplot(data = Bones) + geom_boxplot(aes(Class, Mean.Feret.Diameter..mm., fill=Class))
+ scale_y_log10() + xlab("") + ylab("Mean Feret Diameter (mm)") +
  scale_fill_colorblind() + theme_classic() + theme(axis.title = element_text(size = 15)) +
theme(axis.text = element_text(size = 15))


median(subset(Bones$Mean.Feret.Diameter..mm., Class=="Class I"))
median(subset(Bones$Mean.Feret.Diameter..mm., Class=="Class II"))
wilcox.test(Mean.Feret.Diameter..mm. ~ Class)
#The median Mean Feret Diameter value for Class I (1.015 mm) is significantly
(p=0.0006583) larger than that for Class II (0.87 mm)

#By min feret diameter
ggplot(data = Bones) + geom_boxplot(aes(Class, Min.Feret.Diameter..mm., fill=Class))
+ scale_y_log10() + xlab("") + ylab("Minimum Feret Diameter (mm)") +
  scale_fill_colorblind() + theme_classic() + theme(axis.title = element_text(size = 15)) +
theme(axis.text = element_text(size = 15))

median(subset(Bones$Min.Feret.Diameter..mm., Class=="Class I"))
median(subset(Bones$Min.Feret.Diameter..mm., Class=="Class II"))
```

```
wilcox.test(Min.Feret.Diameter..mm. ~ Class)
  #The median Minimum Feret Diameter for Class I (0.495) is significantly (p=0.004129)
larger than that for Class II (0.460)
```

2.7 References

Abella, J., Martín-Perea, D. M., Valenciano, A., Hontecillas, D., Montoya, P., & Morales, J. (2021). Coprolites in natural traps: direct evidence of bone-eating carnivorans from the Late Miocene Batallones-3 site, Madrid, Spain. *Lethaia*.

Aldridge, R. J., Gabbott, S. E., Siveter, L. J., & Theron, J. N. (2006). Bromalites from the Soom Shale Lagerstätte (Upper Ordovician) of South Africa: palaeoecological and palaeobiological implications. *Palaeontology*, *49*(4), 857-871.

Arnold, J (2021). ggthemes: Extra Themes, Scales and Geoms for 'ggplot2'. R package version 4.2.4.

Autodesk Research "Meshmixer 3D." Computer software. Autodesk, Inc, San Rafal, USA. URL: https://www.meshmixer.com/.

Bajdek, P., Qvarnström, M., Owocki, K., Sulej, T., Sennikov, A. G., Golubev, V. K., & Niedźwiedzki, G. (2016). Microbiota and food residues including possible evidence of pre-mammalian hair in Upper Permian coprolites from Russia. *Lethaia*, *49*(4), 455-477.

Buckland, W. (1822). XVI. Account of an assemblage of fossil teeth and bones of elephant, rhinoceros, hippopotamus, bear, tiger, and hyæna, and sixteen other animals; discovered in a cave at Kirkdale, Yorkshire, in the year 1821: with a comparative view of five similar caverns in various parts of England, and others on the continent. *Philosophical Transactions of the Royal Society of London*, (112), 171-236.

Buckland, W. (1824). *Reliquiae Diluvianae; Or, Observations on the Organic Remains Contained in Caves, Fissures and Diluvial Gravel, and on Other Geological Phenomena, Attesting the Action of an Universal Deluge. By the Rev. William Buckland,...* John Murray, Albemarle-Street.

Buckland, W. (1829). XII.—On the Discovery of Coprolites, or Fossil Fæces, in the Lias at Lyme Regis, and in other Formations. *Transactions of the Geological Society of London*, *2*(1), 223-236.

Buckland, W. (1835). On the discovery of coprolites or fossil faeces in the Lias at Lyme Regis, and in other formations: Transactions of the Geological Society of London, second series, v. 3.

Callen, E. O., & Cameron, T. W. (1955). The diet and parasites of prehistoric Huaca Prieta Indians as determined by dried coprolites. In *Proceedings of the Royal Society of Canada* (Vol. 5, pp. 51-52).

Chin, K., Eberth, D. A., Schweitzer, M. H., Rando, T. A., Sloboda, W. J., & Horner, J. R. (2003). Remarkable preservation of undigested muscle tissue within a Late

Cretaceous tyrannosaurid coprolite from Alberta, Canada. *Palaios*, *18*(3), 286-294.

Chin, K., & Gill, B. D. (1996). Dinosaurs, dung beetles, and conifers: participants in a Cretaceous food web. *Palaios*, 280-285.

Christison, B. E., Gaidies, F., Pineda-Munoz, S., Evans, A. R., Gilbert, M. A., & Fraser, D. (2022). Dietary niches of creodonts and carnivorans of the late Eocene Cypress Hills Formation. *Journal of Mammalogy*, *103*(1), 2-17.

Clark, J., & Guensburg, T. E. (1972). *Arctoid genetic characters as related to the genus Parictis* (Vol. 1150). Field Museum of Natural History.

Di Silvestre, I., Novelli, O., & Bogliani, G. (2000). Feeding habits of the spotted hyaena in the Niokolo Koba National Park, Senegal. *African Journal of Ecology*, *38*(2), 102-107.

Duffin, C. J. (2009). Records of warfare… embalmed in the everlasting hills": a history of early coprolite research. *Mercian geologist*, *17*(2), 101-111.

Farlow, J. O., Chin, K., Argast, A., & Poppy, S. (2010). Coprolites from the Pipe Creek Sinkhole (Late Neogene, Grant County, Indiana, USA). *Journal of Vertebrate Paleontology*, *30*(3), 959-969.

Flynn, J. J., & Galiano, H. (1982). *Phylogeny of early Tertiary Carnivora, with a description of a new species of Protictis from the middle Eocene of northwestern Wyoming*. American Museum of Natural History.

Hanneman, D. L., Lofgren, D., Hasiotis, S. T., & Mcintosh, W. C. (2022). Priabonian, late Eocene chronostratigraphy, depositional environment, and paleosol-trace fossil associations, Pipestone Springs, southwest Montana, USA. *Acta Palaeontologica Polonica*, *67*(1), 5-20.

Häntzschel, W., El-Baz, F., & Amstutz, G. C. (1968). *Coprolites an annotated bibliography* (Vol. 108). Geological Society of America.

Herbig, H. G. (1993). First Upper Devonian crustacean coprolites: Favreina prima n. sp. from Northern Morocco. *Journal of Paleontology*, *67*(1), 98-103.

Hoernes, R. (1904). Über Koprolithen und Enterolithen. *Biologie Centralblatte*, *24*, 566-576.

Horner, J., Hanson, D., (2019). Vertebrate Paleontology of Coprolites. *MBMG Special Publication 122: Geology of Montana. 2*:1-49

Hugot, J. P., Gardner, S. L., Borba, V., Araujo, P., Leles, D., Stock Da-Rosa, Á. A., & Araújo, A. (2014). Discovery of a 240 million year old nematode parasite egg in a cynodont coprolite sheds light on the early origin of pinworms in vertebrates. *Parasites & vectors*, *7*(1), 1-8.

Hunt, R. M. (1974). Daphoenictis, a cat-like carnivore (Mammalia, Amphicyonidae) from the Oligocene of North America. *Journal of Paleontology*, *48*(5), 1030-1047.

Hunt, A. P., & Lucas, S. G. (2012). Classification of vertebrate coprolites and related trace fossils. *New Mexico Museum of Natural History and Science Bulletin*, *57*, 137-146.

Hunt, Adrian., Lucas, Spencer., Milàn, Jesper., & Spielmann, Justin. (2012). Vertebrate coprolite studies: status and prospectus. New Mexico Museum of Natural History and Science. *57*. 5-24.

Hunt, A. P., Milàn, J., Lucas, S. G., & Spielmann, J. A. (Eds.). (2012). *Vertebrate coprolites* (Vol. 57, pp. 153-160). New Mexico Museum of Natural History and Science.

Jouy-Avantin, F., Debenath, A., Moigne, A. M., & Moné, H. (2003). A standardized method for the description and the study of coprolites. *Journal of Archaeological Science*, *30*(3), 367-372.

Kuenzi, W. D., & Fields, R. W. (1971). Tertiary stratigraphy, structure, and geologic history, Jefferson Basin, Montana. *Geological Society of America Bulletin*, *82*(12), 3373-3394.

Kruuk, H. (1972). *The spotted hyena: a study of predation and social behavior* (No. Sirsi) a102104).

LaGarry, H. E. (2004). *Taphonomic evidence of bone processing from the Oligocene of northwestern Nebraska*. School of Natural Resources, Institute of Agriculture and Natural Resources, University of Nebraska-Lincoln.

Landini G. (2006-2020) Background illumination correction. Available at: https://blog.bham.ac.uk/intellimic/background-illumination-correction

Leidy, J. O. S. E. P. H. (1853). Remarks on a collection of fossil Mammalia from Nebraska. *Proceedings of the Academy of Natural Sciences of Philadelphia*, *6*, 392-394.

Lofgren, D. L., Shen, C. Y., Buday, N. N., Ylagan, C. A., Lofgren, K. K., Lai, R., ... & Tabrum, A. R. (2017). Coprolites and mammalian carnivores from Pipestone Springs, Montana, and their paleoecological significance. *Annals of Carnegie Museum*, *84*(4), 265-285.

Loud, L. L. and Harrington, M. R., (1929), Lovelock Cave: *University of California Publications in American Archaeology and Ethnology*, *25*, 183

Magondu, B. W. (2021). Fracture Mechanics of Pelleted Feces Within Mammals.

Martin, P. S., Sabels, B. E., & Shutler, D. (1961). Rampart Cave coprolite and ecology of the Shasta ground sloth. *American Journal of Science*, *259*(2), 102-107.

Martin, L. D. (1989). Fossil history of the terrestrial Carnivora. In *Carnivore behavior, ecology, and evolution* (pp. 536-568). Springer, Boston, MA.

Mellett, J. S. (1977). *Paleobiology of North American Hyaenodon (Mammalia, Creodonta)*. Karger Publishers.

Meng, J., & Wyss, A. R. (1997). Multituberculate and other mammal hair recovered from Palaeogene excreta. *Nature*, *385*(6618), 712-714.

Munsell Color (Firm). (2010). Munsell soil color charts: with genuine Munsell color chips. Grand Rapids, MI: Munsell Color,

Neumayer, L. (1904). Die Koprolithen des Perm von Texas: *Palaeontographica*, v. 51.

Northwood, C. (2005). Early Triassic coprolites from Australia and their palaeobiological significance. *Palaeontology*, *48*(1), 49-68.

ORS: Object Research Systems. (2020). Dragonfly software v. 2020.2 Build 941v. 2022.1, Montréal, Canada.URL: https://www.theobjects.com/dragonfly/new.html

Pokines, J. T. and Tersigni-Tarrant, M. A. (2012). Forensic anthropology: an introduction. In: Tersigni-Tarrant, M. A. & Shirley, N. R. (eds) Forensic Anthropology: An Introduction. CRC Press.

Pratt, B. R. (1998). Molar-tooth structure in Proterozoic carbonate rocks: Origin from synsedimentary earthquakes, and implications for the nature and evolution of basins and marine sediment. *Geological Society of America Bulletin*, *110*(8), 1028-1045.

Prothero, D. R. (1984). Magnetostratigraphy of the early Oligocene Pipestone Springs locality, Jefferson County, Montana. Contributions to Geology, University of Wyoming, 23, 33–36.

Prothero, D. R., & Emry, R. J. (1996). *The Terrestrial Eocene-Oligocene Transition in North America* (p. 704).

R Core Team. (2017). R: A language and environment for statistical computing. R Foundation for Statistical Computing, Vienna, Austria. URL: https://www.R-project.org/.

Roust, N.L. (1967). Preliminary Examination of Prehistoric Human Coprolites from Four Western Nevada Caves. *Papers in Great Basin Archaeology, University of California Archaeological Survey Report* 70, 49-88.

Scott, W.B. (1898). Notes on the Canidae of the White River Oligocene. *Proceedings of the American Philosophical Society*, 19:327–415.

Scott, W. B., & Jepsen, G. L. (1936). The mammalian fauna of the White River Oligocene: part I. Insectivora and Carnivora. *Transactions of the American Philosophical Society*, *28*(1), 1-153.

Smith, R. M., & Botha-Brink, J. (2011). Morphology and composition of bone-bearing coprolites from the late Permian Beaufort Group, Karoo Basin, South Africa. *Palaeogeography, Palaeoclimatology, Palaeoecology*, *312*(1-2), 40-53.

Shillito, L. M., Blong, J. C., Green, E. J., & van Asperen, E. N. (2020). The what, how and why of archaeological coprolite analysis. *Earth-Science Reviews*, *207*, 103196.

Sutton, M., Rahman, I. A. & Garwood, R. J. (2013). Techniques for Virtual Palaeontology. Sutton, M., Rahman, I. A. & Garwood, R. J. (eds). Wiley-Blackwell pp. 247.

Tabrum, A. R., Prothero, D. R., Garcia, D., & Emry, R. J. (1996). Magnetostratigraphy and biostratigraphy of the Eocene-Oligocene transition, southwestern Montana. *The Terrestrial Eocene-Oligocene transition in North America*, 278-311.

Tafforeau, P., Boistel, R., Boller, E., Bravin, A., Brunet, M., Chaimanee, Y., & Zabler, S. (2006). Applications of X-ray synchrotron microtomography for non-destructive 3D studies of paleontological specimens. *Applied Physics A*, *83*(2), 195-202.

Taru, P., & Backwell, L. (2013). Identification of fossil hairs in Parahyaena brunnea coprolites from Middle Pleistocene deposits at Gladysvale cave, South Africa. *Journal of archaeological science*, *40*(10), 3674-3685.

Thulborn, R. A. (1991). Morphology, preservation and palaeobiological significance of dinosaur copralites. *Palaeogeography, Palaeoclimatology, Palaeoecology*, *83*(4), 341-366.

Turk, J., Čretnik, J., Turk, M., & Mladenovič, A. (2015). Hair imprints in Pleistocene cave sediments and the use of X-ray micro-computed tomography for their reconstruction. *Facies*, *61*(1), 1-11.

Verde, M. (2003). Mammalian carnivore coprolites from the Sopas Formation (upper Pleistocene, Lujanian stage), Uruguay. *Ichnos*, *9*(1-2), 77-80.

Wang, X., White, S. C., Balisi, M., Biewer, J., Sankey, J., Garber, D., & Tseng, Z. J. (2018). First bone-cracking dog coprolites provide new insight into bone consumption in Borophagus and their unique ecological niche. *Elife*, *7*, e34773.

Wickman, H. (2016). ggplot2: Elegant Graphics for Data Analysis. Springer-Verlag New York,

Williams, M. E. (1972). The origin of" spiral coprolites".

Zangerl, R., & Richardson, E. S. (1963). The paleoecological history of two Pennsylvanian black shales.